Universität Hamburg

Synchrotron Research Institute

YEREVAN STATE UNIVERSITY

German-Armenian Joint Practical Course
on Accelerator Physics

Accelerator Magnets and Magnetic Field Measurement

Supervisor: Dr. Vitali Khachatryan

PIER
Partnership of
Universitat Hamburg and DESY

YEREVAN, ARMENIA
2025

CONTENTS

Introduction

In particle accelerator facilities charged particle beams are being controlled and manipulated by various types of magnets. Bending magnets, as well as corrector magnets are used for the beam guidance and steering. Beam focusing is realized by applying solenoid and several quadrupole magnets in doublet and triplet arrangements. Finally, light with specific properties will be produced through the periodic magnetic structure, the undulator.

Solenoid magnets are used for focusing low energy particle beams. Unlike with optical lenses, the image is rotated with respect to the object. Since the focal length increases with the square of the momentum, a solenoid lens is effective only for small momenta. Iron cover of the solenoid provides a return path for the solenoid field, thus enhancing and concentrating the field inside the magnet gap which is seen by the particle beam. In contrast to the solenoid, the quadrupole magnet focuses the beam only in one plane. If it focuses the beam in the horizontal plane, then the beam is being defocused in the vertical plane and vice versa.

Experimental tasks include: 1) Mapping of the axial magnetic field along the central axis of the quadrupole magnet using HALL probes; 2 Demonstration of focusing effect of the solenoid magnet by variation of the magnet current and observation of beam profile on the YAG scintillation screen. Demonstration of the beam bending by dipole magnet by registration of beam using Faraday cup and YAG scintillation screen station.

1 Mathematical fundamentals

A simple expression, satisfying Laplace's equation $\nabla^2 F = \left(\frac{\partial}{\partial x^2} + \frac{\partial}{\partial y^2}\right) F = 0$, fully characterizing the two dimensional magnetic field in the absence of iron and current (in the air region) is $F = z^n$ where $z = x + iy$ is the complex space coordinate.

Taking the derivatives;

$\frac{\partial F}{\partial x} = \frac{\partial F}{\partial z}\frac{dz}{dx} = nz^{n-1}\frac{dz}{dx}$ But $\frac{dz}{dx} = 1$. Therefore, $\frac{\partial F}{\partial x} = nz^{n-1}$.

$\frac{\partial^2 F}{\partial x^2} = \frac{\partial (nz^{n-1})}{\partial z}\frac{dz}{dx} = n(n-1)z^{n-2}$.

$\frac{\partial F}{\partial y} = \frac{\partial F}{\partial z}\frac{dz}{dy} = nz^{n-1}\frac{dz}{dy}$. But $\frac{dz}{dy} = i$. Therefore, $\frac{\partial F}{\partial y} = nz^{n-1}\frac{dz}{dy}i$.

$$\frac{\partial^2 F}{\partial y^2} = \frac{\partial (nz^{n-1})}{\partial z}\frac{dz}{dy} = n(n-1)z^{n-2}i^2 = -n(n-1)z^{n-2}$$

Substituting $\nabla^2 F = \frac{\partial^2 F}{\partial x^2} + \frac{\partial^2 F}{\partial y^2} = n(n-1)z^{n-2} - n(n-1)z^{n-2} = 0$.

Therefore, $F = z^n$ satisfies Laplace's equation. Moreover, $F = C_n z^n$ and $F = \sum_{n=1}^{N} C_n z^n$where, in general,$C_n$ is a complex constant also satisfy Laplace's equation.

1.1 Multipole expansions

In this section we denote the vertical coordinate by y instead of z because we want to keep the conventional notation $z = x + iy$ for complex numbers.
The length of modern accelerator magnets is usually much larger than their bore radius. The end field contribution is then rather small and the magnetic field has to a good approximation only transverse components. (This section relays heavily on the source [Rossbach, P. Schmüser, Basic course on accelerator optics, DESY-M-93-02.].)
For two-dimensional fields one can apply the theory of analytic functions. From
div **B** = 0

it follows that a vector potential **A** exists such that

B = rot **A** (1.1)

Because of the transversality of the field, the vector potential has only a component A_s in the longitudinal direction s. In vacuum, for example inside the beam pipe, we have furthermore (for static fields)

rot **B** = 0

This implies that **B** can also be written as the gradient of a scalar potential V:

B = – *grad* V (1.2)

Combining both equations (1.1, 1.2) we get:

$$B_x = -\frac{\partial V}{\partial x} = \frac{\partial A_s}{\partial y} \qquad B_y = -\frac{\partial V}{\partial y} = -\frac{\partial A_s}{\partial x} \tag{1.3}$$

Now we define a complex potential function of $z = x + iy$ by $\tilde{A}(z) = A_s(x,y) + i\,V(x,y)$.

The equations (1.3) are just the Cauchy-Riemann conditions for the real and imaginary part of an analytic function. So the complex potential is an analytic function and can be expanded in a power series

$$\tilde{A}(z) = \sum_{n=0}^{\infty} \kappa_n z^n \qquad \kappa_n = \lambda_n + i\,\mu_n \tag{1.4}$$

with λ_n, μ_n real constants.
From complex analysis we know that this series expansion converges for all z inside a circle $|z| < r_c$. The radius of convergence r_c is the closest distance between the origin of the expansion and the iron yoke or the coil where the Eqs. (1.3) break down and $\tilde{A}(z)$ is no more analytic, see Fig. 1.1.

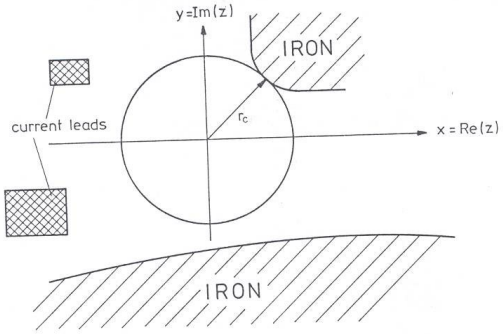

Figure 1.1: The multipole expansion with respect to $z = 0$ is only valid inside the circle r_c (radius of convergence).

Cylindrical coordinate representation

For superconducting magnets, it is practical to express the field in cylindrical coordinates (r, φ, s), see Fig. 1.2:

$$x = r\cos\varphi \qquad y = r\sin\varphi \qquad z^n = r^n \cdot e^{in\varphi} = r^n(\cos n\varphi + i \sin n\varphi) \tag{1.5}$$

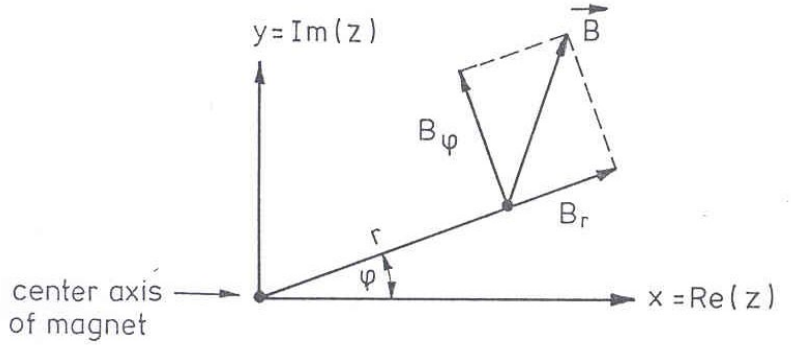

Figure 1.2: Cylindrical coordinate system used in the multipole expansion.

The scalar potential is given by the imaginary part of Eq. (1.4)

$$V(r,\varphi) = \sum_{n=0}^{\infty} (\mu_n \cos n\varphi + \lambda_n \sin n\varphi)\, r^n \tag{1.6}$$

Similarly, we get from the real part of Eq. (1.4)

$$A_s(r,\varphi) = \sum_{n=0}^{\infty} (\lambda_n \cos n\varphi - \mu_n \sin n\varphi)\, r^n \tag{1.7}$$

Taking the gradient of $-V(r,\varphi)$, we get the multipole expansion of the azimuthal and radial field components, respectively

$$B_\varphi = -\frac{\partial V}{r\partial\varphi} = -\sum_{n=1}^{\infty} n\left(\lambda_n \cos(n\varphi) - \mu_n \sin(n\varphi)\right) r^{n-1}$$

$$B_r = -\sum_{n=1}^{\infty} n(\mu_n \cos n\varphi + \lambda_n \sin n\varphi)\, r^{n-1}$$

Now it is convenient to define a `reference radius' r_0 for the multipole expansion and to denote the magnitude of the main field component of the magnet in question by B_{main}. *A* useful choice for r_0 is the largest conceivable deviation of beam particles from the design orbit (25 mm in HERA, that is the inner radius of the beam pipe). Furthermore we introduce the **'normal'** multipole coefficients b_n and the **'skew'** coefficients a_n by

$$b_n = -\frac{n\lambda_n}{B_{\text{main}}} r_0^{n-1} \qquad a_n = +\frac{n\mu_n}{B_{\text{main}}} r_0^{n-1} \tag{1.8}$$

Then the multipole expansions read (note that a_0, b_0 are set to zero as they don't contribute to the magnetic field)

$$V(r,\varphi) = -B_{\text{main}} r_0 \sum_{n=1}^{\infty} \left(-\frac{a_n}{n} \cos n\varphi + \frac{b_n}{n} \sin n\varphi \right) \left(\frac{r}{r_0} \right)^n \tag{1.9}$$

$$A_s(r,\varphi) = -B_{\text{main}} r_0 \sum_{n=1}^{\infty} \left(\frac{b_n}{n} \cos n\varphi + \frac{a_n}{n} \sin n\varphi \right) \left(\frac{r}{r_0} \right)^n \tag{1.10}$$

$$B_\varphi(r,\varphi) = B_{\text{main}} \sum_{n=1}^{\infty} \left(b_n \cos n\varphi + a_n \sin n\varphi \right) \left(\frac{r}{r_0} \right)^{n-1} \tag{1.11}$$

$$B_r(r,\varphi) = B_{\text{main}} \sum_{n=1}^{\infty} \left(-a_n \cos n\varphi + b_n \sin n\varphi \right) \left(\frac{r}{r_0} \right)^{n-1} \tag{1.12}$$

Remember that these multipole expansions are only valid within a circle of radius r_c containing neither iron nor current! For an ideal $2n$-pole magnet we have b_n=1 and all other $a_n, b_n = 0$. We call

$n = 1$ Dipole
$n = 2$ Quadrupole
$n = 3$ Sextupole

It is instructive to consider $B_\varphi + iB_r$:

$$B_\varphi + iB_r = B_{\text{main}} \sum_{n=1}^{\infty} \left(\frac{r}{r_0} \right)^{n-1} \left[b_n \left(\cos n\varphi + i \sin n\varphi \right) - i a_n \left(\cos n\varphi + i \sin n\varphi \right) \right]$$

$$B_\varphi + iB_r = B_{\text{main}} \sum_{n=1}^{\infty} \left(\frac{r}{r_0} \right)^{n-1} (b_n - i a_n) e^{in\varphi} \tag{1.13}$$

Thus

$$(|\boldsymbol{B}|)_n = \left(\sqrt{B_r^2 + B_\varphi^2} \right)_n = B_{\text{main}} \left(\frac{r}{r_0} \right)^{n-1} \sqrt{a_n^2 + b_n^2} \tag{1.14}$$

i.e. the magnitude of the 2*n* pole field component *does not* depend on the azimuth and scales with the $(n-1)$th power of *r*. Equation (1.14) also illustrates a simple interpretation of the fractional multipole field coefficients a_n, b_n : They are just the relative field contribution of the *n*th multipole to the main field at the reference radius r_0 . This is the reason why the coefficients λ_n, μ_n have been normalized with Eqs. (1.8).

Conventional accelerator magnets with iron pole shoes are limited to dipole fields of about 2 T and quadrupole gradients of about 20 T/m. Significantly higher values (> 6 T, > 100 T/m) are possible with superconducting magnets. In these magnets the field distribution is entirely determined by the conductor arrangement and the coils have to be built with extreme accuracy to keep field distortions below the required level of 10^{-4}. Figure 15a shows schematically the layout of a superconducting dipole.

In iron-free magnets the field distribution generated by an azimuthal current distribution described by $dI(\varphi) = I_0 \cos(n\varphi) d\varphi$ is given by

$$B_r = -\frac{\mu_0 I_0}{2r_0}\left(\frac{r}{r_0}\right)^{n-1} \sin(n\varphi)$$

$$B_\varphi = -\frac{\mu_0 I_0}{2r_0}\left(\frac{r}{r_0}\right)^{n-1} \cos(n\varphi)$$

Ideally, the current as a function of the azimuthal angle φ should follow a $\cos\varphi$-distribution to generate a pure dipole field and a $\cos 2\varphi$ ($\cos 3\varphi$) distribution for a quadrupole (sextupole) field. Since these ideal distributions are technically difficult to realize one approximates them by an arrangement of current shells. The cylindrical coordinate representation is particularly useful for magnet design from current shells.

Another application of the cylindrical coordinate representation is the technique of measurement of the multipole components with a coil rotating in the field: The *n*th Fourier component of the induced voltage is proportional to $\sqrt{a_n^2 + b_n^2}$ while its phase is related to a_n/b_n.

In a good dipole or quadrupole magnet the unwanted multipole coefficients a_n, b_n are typically a few 10^{-4} or less.

Finally it is noted that within the cylindrical coordinate representation one easily understands which multipole components are forbidden if specific symmetry properties of the field are assumed. For instance, for a quadrupole with perfect constructional symmetry only *odd* harmonics of the 4-pole are allowed. Or, as another example, if mirror symmetry with respect to the $x - s$ plane is assumed, all skew components are forbidden since B_φ must behave purely cos-like. A similar reasoning shows that any normal 2*n*-pole magnet transforms into a skew 2*n*-pole magnet if rotated by $\pi/2n$.

Cartesian coordinates

In cartesian coordinates, Eq. (1.4) reads

$$A_s(x,y) + i\, V(x,y) = \sum_{n=0}^{\infty} \kappa_n z^n = \sum_{n=o}^{\infty} (\lambda_n + i\mu_n)(x+iy)^n \qquad (1.15)$$

Separation of real and imaginary part and use of Eq. (1.8) yields

$$A_s(x,y) = \Re \sum_{n=0}^{\infty} k_n z^n = -B_{\text{main}} \left[b_1 x + a_1 y + \frac{b_2}{2r_o}(x^2 - y^2) + \frac{a_2}{r_0} xy + \frac{b_3}{3r_0^2}(x^3 - 3xy^2) + \right.$$

$$\left. + \frac{a_3}{3r_0^2}(3x^2y - y^3) + \frac{b_4}{4r_0^3}(x^4 - 6x^2y^2 + y^4) + \frac{a_4}{r_0^3}(x^3y - xy^3) \pm \ldots \right] \qquad (1.16)$$

$$V(x,y) = \Im \sum_{n=0}^{\infty} \kappa_n z^n = B_{\text{main}} [a_1 x - b_1 y + \frac{a_2}{2r_0}(x^2 - y^2) - \frac{b_2}{r_0} xy + \frac{a_3}{3r_0^2}(x^3 - 3xy^2) -$$

$$- \frac{b_3}{3r_0^2}(3x^2y - y^3) + \frac{a_4}{4r_0^3}(x^4 - 6x^2y^2 + y^4) - \frac{b_4}{r_0^3}(x^3y - xy^3) \pm \ldots] \qquad (1.17)$$

To get the cartesian components of the magnetic field we now have to take the gradient of $-V(x,y)$ in cartesian coordinates, see Eq. (1.3)

$$B_x(x,y) = -\frac{\partial V}{\partial x} = B_{\text{main}} \left[-a_1 + \frac{b_2}{r_0} y - \frac{a_2}{r_0} x - \frac{a_3}{r_0^2}(x^2 - y^2) + \frac{b_3}{r_0^2} 2xy - \right.$$

$$\left. - \frac{a_4}{r_0^3}(x^3 - 3xy^2) + \frac{b_4}{r_0^3}(3x^2y - y^3) \pm \ldots \right] \qquad (1.18)$$

$$B_y(x,y) = -\frac{\partial V}{\partial y} = B_{\text{main}} \left[b_1 + \frac{a_2}{r_0} y + \frac{b_2}{r_0} x + \frac{a_3}{r_0^2} 2xy + \frac{b_3}{r_0^2}(x^2 - y^2) + \right.$$

$$\left. + \frac{a_4}{r_0^3}(3x^2y - y^3) + \frac{b_4}{r_0^3}(x^3 - 3xy^2) \pm \ldots \right] \qquad (1.19)$$

Another useful combination of Eqs. (1.18) and (1.19) is

$$B_y + i\, B_x = -\frac{\partial}{\partial z}(A_s + i\, V) = -\sum_{n=1}^{\infty} n\ (\lambda_n + i\, \mu_n)\ (x+iy)^{n-1}$$

$$B_y + i\, B_x = B_{\text{main}} \sum_{n=1}^{\infty}\ (b_n - i a_n)\left(\frac{x}{r_0} + i\frac{y}{r_0}\right)^{n-1}$$

Here are two applications of the cartesian representation of multipoles:

1) If the motion of particles is described in cartesian coordinates, the contribution of each individual multipole to the equation of motion is easily identified. As stated before, the coefficients b_n are called the "normal" multipole coefficients, a_n are the "skew" coefficients. In magnets containing normal coefficients only, a flat beam (i.e. no vertical extension) remains flat forever, since for $y \equiv 0$ there is $B_x \equiv 0$, i.e. no vertical force. Thus, there is no coupling of horizontal motion into the vertical.

2) Equation (1.17) is useful in conventional lens design work with iron pole shoes. It describes the pole contours of dipole-(n = 1), quadrupole-(n = 2), sextupole-(n = 3), octupole-(n = 4), etc., magnets, because the pole contour is a line of constant magnetic potential. The pole contour of a normal quadrupole (b_2), for instance, is given by the hyperbola $x \cdot y$ = const (see Eq. (2.5)).

Finally, we show explicitly the field distribution of the most important multipole components:

Normal dipole (n = 1):	$b_1 \cdot B_{main} = B_{vert}$ (horizontally bending)
$B_\varphi(r,\varphi) = B_{vert} \cdot \cos\varphi$	$B_r(r,\varphi) = B_{vert} \cdot \sin\varphi$
$B_x(x,y) = 0$	$B_y(x,y) = B_{vert}$

Skew dipole (n = 1):	$a_1 \cdot B_{main} = B_{hor}$ (vertically bending)
$B_\varphi(r,\varphi) = B_{hor} \cdot \sin\varphi$	$B_r(r,\varphi) = -B_{hor} \cdot \cos\varphi$
$B_x(x,y) = -B_{hor}$	$B_y(x,y) = 0$

Normal quadrupole (n = 2):	$b_2 \cdot B_{main} = -g \cdot r_0$ (where g is the gradient)
$B_\varphi(r,\varphi) = -g\, r \cos 2\varphi$	$B_r(r,\varphi) = -g\, r \sin 2\varphi$
$B_x(x,y) = -g\, y$	$B_y(x,y) = -g\, x$

2 Accelerator magnets

The modern particle accelerators are equipped with dipole magnets for beam deflection and quadrupoles for beam focusing. Soft iron of high permeability is used to concentrate the field into the small region where it is needed. This also reduces electric power consumption and easily allows to provide high field quality. In those cases where the required field strength is either very small ($B << 0.1T$) or above the saturation level ($B > 2\,T$), "air coil" magnets are used. (This section relays heavily on the source [Rossbach, P. Schmüser, Basic course on accelerator optics, DESY-M-93-02.].)

2.1 Dipole magnet

A magnet with flat pole faces generates a homogeneous field B(**Fig. 2.1**).

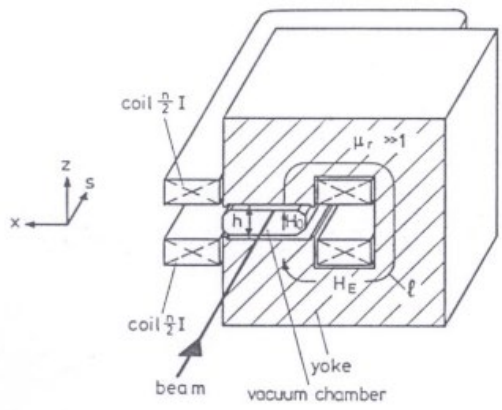

Figure 2.1: Schematic view of a dipole magnet

The field is computed from the formula

$$\oint \boldsymbol{H} \cdot \boldsymbol{ds} = hH_0 + lH_E = nI$$

$$H_E = \frac{1}{\mu_r} \cdot H_0$$

For $\mu_r \gg 1$ we obtain

$$B_0 = \frac{\mu_0 nI}{h}; \;\; h = gap\ height \tag{2.1}$$

Formula (2.1) is only approximate. In particular it neglects fringe fields and iron saturation. The radius of curvature for a particle of charge e and momentum p is given by

$$\frac{1}{\rho}[m^{-1}] = \frac{eB_0}{p} = 0.2998 \frac{B_0[T]}{p[GeV/c]} \tag{2.2}$$

2.2 Solenoid lens

A relatively simple magnetic lens arises from the magnetic field of a rotationally symmetric coil, see **Fig. 2.2**.

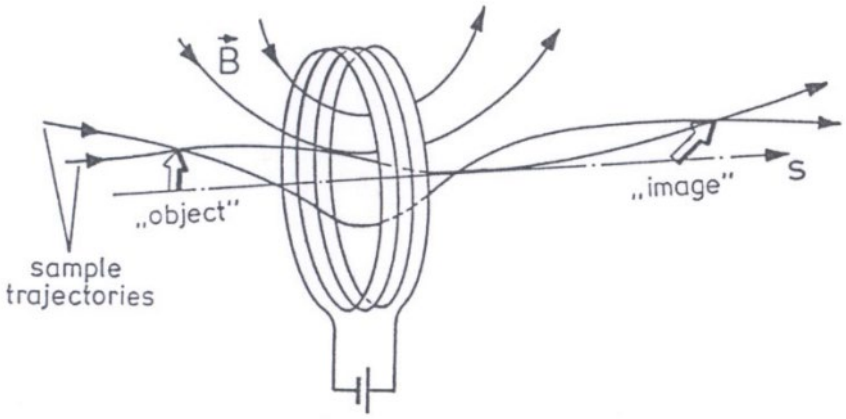

Figure 2.2: Particle trajectories and field lines in a "thin" lens formed by the solenoid

Due to the Maxwell equation $div\boldsymbol{B} = 0$, the magnetic field, which is purely longitudinal in the inner part of the coil, must contain radial components in the outer part. While particles moving exactly on the axis do not experience any force, the others suffer an azimuthal acceleration due to the radial component while entering and leaving the lens. Because of the azimuthal motion there is a radial force in the longitudinal field. As required for imaging, this force is, indeed, proportional to the radial distance r if r does not change too much during the passage of the lens. To increase the field close to the axis and to concentrate it into a small area, the coil is usually surrounded by an iron yoke. The focal length f_{sol} is given by

$$\frac{1}{f_{sol}} = \int \left(\frac{eB_s}{2p}\right)^2 ds \tag{2.3}$$

In contrast to optical lenses, the image is rotated with respect to the object. As seen from **Eq. (2.3)**, f_{sol} increases with the square of the momentum p. Therefore a solenoid lens is

effective for small momenta only. At $>> 1\,MeV/c$, a quadrupole magnet is a much more effective lens.

2.4 Quadrupole magnet

Quadrupole magnets have four iron pole shoes with hyperbolic contour (**Fig. 2.3**).

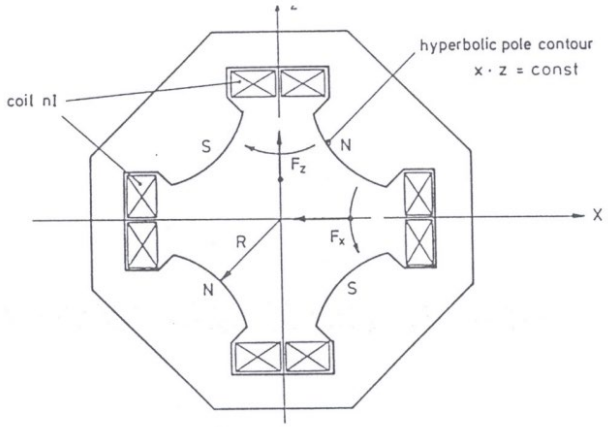

Figure 2.3: Cross-section of a quadrupole magnet.

With the polarity shown, the horizontal component of the Lorentz force on a positively charged particle, moving into the plane of the drawing, is directed towards the axis, the vertical component is directed away from the axis. The magnet shown is thus horizontally focusing, vertically defocusing. The opposite holds when the current direction, the particle charge or its direction of motion is reversed.

The field is linear in the deviation from the axis:

$$B_z = -gx; \qquad B_x = -gz \tag{2.4}$$

In the air space of the magnet which contains neither iron nor current conductors we have the Maxwell equation

$$\nabla \times \boldsymbol{B} = 0 \tag{2.5}$$

Here the field can be written as the gradient of a potential

$$\boldsymbol{B} = -\nabla V \text{ with } V(x,z) = gxz \tag{2.6}$$

The equipotential lines are the hyperbolas $xz = const$. The field lines are perpendicular to them. If the relative permeability of the iron is large,$\mu_r >> 1$, iron pole shoes with hyperbolic contour generate a rather pure quadrupole field (2.4).

The gradient g and the current I in the coils can be related by the integral theorem

$$\oint \boldsymbol{H} \cdot \boldsymbol{ds} = nI \tag{2.7}$$

The path of integration is shown in **Fig. 2.4**.

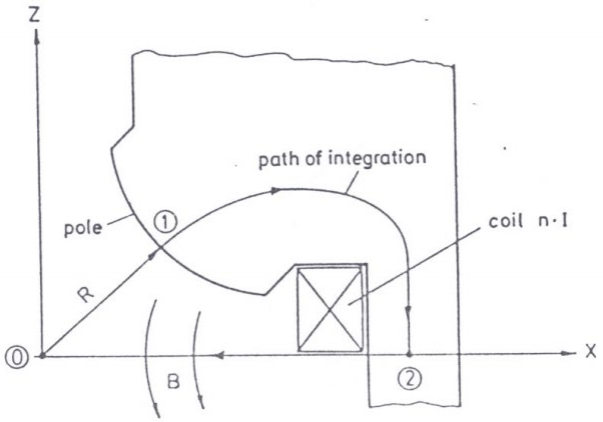

Figure 2.4: Path of integration used to compute the quadrupole gradient as a function of the current

$$nI = \oint Hds = \int_0^R H(r)dr + \int_1^2 H_E \cdot ds + \int_2^0 H \cdot ds \tag{2.8}$$

On the first path $H(r) = gr/\mu_r$. The second integral is very small for $\mu_r >> 1$. The third integral vanishes identically since $\boldsymbol{H} \perp \boldsymbol{ds}$. So we get in good approximation

$$nI = \frac{1}{\mu_0} \int_0^R g\, r\, dr \qquad r = \sqrt{x^2 + z^2} \tag{2.9}$$

$$g = \frac{2\mu_0 nI}{R^2} \tag{2.10}$$

In analogy to the bending strength $1/\rho$ of a dipole magnet, it is convenient to relate the field gradient to its optical effect. To this end, the field gradient is normalized to the momentum of the particle, thus defining the quadrupole strength

$$k = \frac{eg}{\rho} \tag{2.11}$$

Numerically

$$k[m^2] = 0.2998 \frac{g[T/m]}{\rho[GeV/c]} \tag{2.12}$$

If l denotes the length of the quadrupole, its focal length f is given by

$$\frac{1}{f} = k \cdot l \tag{2.13}$$

Generally, a lens with $f >> l$ is called a "thin lens" -irrespective of the absolute value of l. An interesting property of the quadrupole is that the horizontal force component depends only on the horizontal position and not on the vertical position of the particle trajectory. Similarly, the vertical component of the Lorentz force depends only on the vertical position.

$$F_x = evB_z(x,z) = -evgx \quad ; F_z = -evB_x(x,z) = evgz \tag{2.14}$$

The important consequence is that in a so-called *linear machine*, containing only dipole and quadrupole fields, the horizontal and vertical betatron oscillations are completely *decoupled*.

2.5 Particle tracks and transformation matrices

The ideal orbit of a particle in the accelerator determined by the construction of the accelerator is called the reference orbit. In order to determine the motion of the particles, we first set up the general equation of motion in the moving coordinate system $K = \{x, y, z\}$. The derivation can be found. The linear equations of motion for the particles are

$$x''(z) + \left(\frac{1}{R^2(z)} - k(z)\right)x(z) = \frac{1}{R(z)}\frac{\Delta p}{p}$$
$$y''(z) + k(z)y(z) = 0 \tag{2.15}$$

where p denotes the reference momentum of the particles, Δp the momentum deviation, $R\,(z)$ the curvature radius and $k\,(z)$ the quadrupole strength. The coordinate z denotes the distance traveled along the nominal path and here is the independent variable, i. she takes on the role of the time. The general solution of the equation of motion is a linear combination of a cosine-like $C\,(z)$ and a sinusoidal term $S\,(z)$ as well as a dispersion term $D_x\,(z)$ describing the momentum-dependent part of the motion.

$$x(z) = C(z)x_0 + S(z)x_0' + D_x(z)\frac{\Delta p}{p_0}$$
$$y(z) = C(z)y_0 + S(z)y_0' \tag{2.16}$$

where $x_0 = x\,(0)$, or $y_0 = y\,(0)$ the initial values of the horizontal or vertical positions and $x_0' = x'\,(0)$, and $y_0' = y'\,(0)$ arethe initial values of the horizontal or vertical vertical angle to the nominal path. Here we assume a plane setpoint trajectory such that $D_y = D_y' = 0$. The trajectory equation can be solved analytically if the curvature radius $\rho\,(z)$ and the quadrupole strength $k\,(z)$ are constant. This is the case within individual components of beam guidance such as drift paths, dipole magnets and quadrupole magnets. The mapping of the particle coordinates from the beginning to the end of the component $(x, x')_0 \rightarrow (x, x')_z$ is then a linear transformation that can also be described using transfer matrices.

$$\begin{pmatrix} x \\ x' \\ \Delta p/p_0 \end{pmatrix} = \begin{pmatrix} C & S & D_x \\ C' & S' & D_x' \\ 0 & 0 & 1 \end{pmatrix}\begin{pmatrix} x \\ x' \\ \Delta p/p_0 \end{pmatrix}$$
$$\begin{pmatrix} y \\ y' \\ \Delta p/p_0 \end{pmatrix} = \begin{pmatrix} C & S & 0 \\ C' & S' & 0 \\ 0 & 0 & 1 \end{pmatrix}\begin{pmatrix} y \\ y' \\ \Delta p/p_0 \end{pmatrix} \tag{2.17}$$

The matrix elements are constants that depend only on k, R and the length L of the component. The transfer matrix for a complete beam transport is the product of the transfer matrices of individual beam transport components. To simplify the derivation, we assume that the magnetic fields at the input and output of the component follow a step function [2].

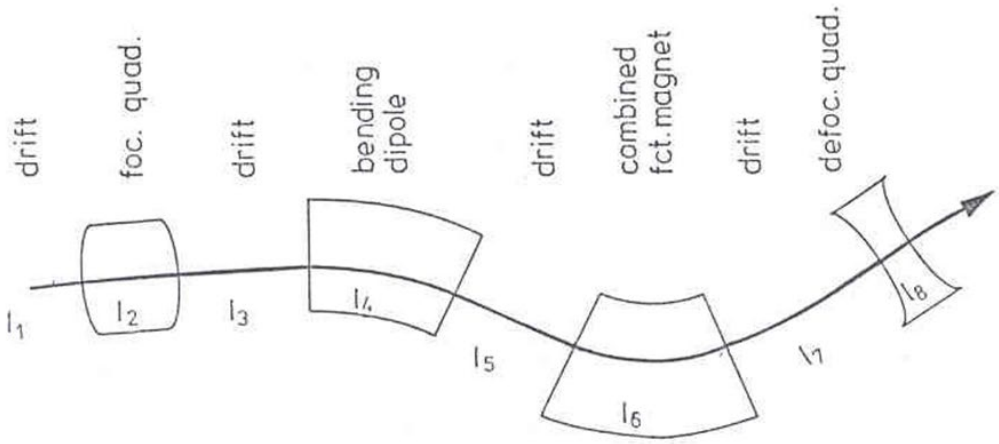

Figure 2.5: The complete transfer matrix of this sequence of magnetic elements is the matrix product $M_{tot} = M_8 \cdot M_7 \cdot M_6 \cdot M_5 \cdot M_4 \cdot M_3 \cdot M_2 \cdot M_1$. Each of the matrices $M_1 \ldots M_8$ decribes a section with K(s) = const.

2.6 Drift

In a drift path, no external force acts on the particles. The transformation matrix depends only on the length L of the drift path.

$$\frac{1}{R} = 0 = k \Rightarrow M_x = M_y = R_{drift} = \begin{pmatrix} 1 & L & 0 \\ 0 & 1 & 0 \\ 0 & 0 & 1 \end{pmatrix} \tag{2.18}$$

2.7 Dipole magnet

A dipole magnet whose field boundaries at the input and output are at right angles to the reference orbit is called the sector magnet (see Figure 2.6).

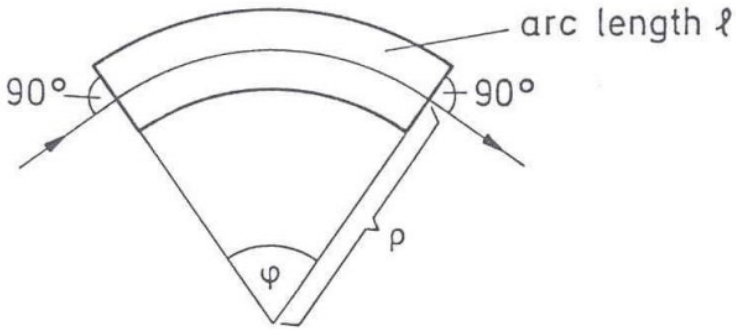

Figure 2.6: Schematic structure of a sector magnet with deflection radius ρ .

$$k = 0; \quad \alpha = \frac{l}{R} \Rightarrow M_x = R_{dipol} = \begin{pmatrix} \cos\alpha & R\sin\alpha & R(1-\cos\alpha) \\ -\frac{1}{R}\sin\alpha & \cos\alpha & \sin\alpha \\ 0 & 0 & 1 \end{pmatrix} \tag{2.19}$$

$$M_y = R_{drift} = \begin{pmatrix} 1 & L & 0 \\ 0 & 1 & 0 \\ 0 & 0 & 1 \end{pmatrix} \tag{2.20}$$

2.8 Rectangular dipole magnet

In practice, dipole magnets are often built straight with the magnet end plates not perpendicular to the central trajectory. A rectangular magnet can be derived from a sector magnet by superimposing at the entrance and exit a "magnetic wedge" of angle $\delta = \varphi/2$, as shown in Fig. 2.7.

Figure 2.7: Rectangular dipole magnet and horizontally defocusing magnetic wedge

The deflection angle in the magnetic wedge is

$$\alpha = \frac{\Delta l}{\rho} = \frac{x\,tan\delta}{\rho} = \frac{x}{f} \tag{2.21}$$

It acts as a thin defocusing lens with $1/f = (\tan\delta)/\rho$ in the horizontal plane, as a focusing length with the same strength in the vertical plane. The horizontal transformation matrix for a rectangular magnet is

$$M_x = \begin{pmatrix} 1 & 0 & 0 \\ \frac{1}{\rho}\tan\delta & 1 & 0 \\ 0 & 0 & 1 \end{pmatrix} \begin{pmatrix} \cos\varphi & \rho\sin\varphi & \rho(1-\cos\varphi) \\ -\frac{1}{\rho}\sin\varphi & \cos\varphi & \sin\varphi \\ 0 & 0 & 1 \end{pmatrix} \begin{pmatrix} 1 & 0 & 0 \\ \frac{1}{\rho}\tan\delta & 1 & 0 \\ 0 & 0 & 1 \end{pmatrix} \tag{2.23}$$

For $\varphi \ll 1$, $\delta = \varphi/2$:

$$M_x = \begin{pmatrix} 1 & \rho sin\varphi & \rho(1-cos\varphi) \\ 0 & 1 & 2\tan\varphi/2 \\ 0 & 0 & 1 \end{pmatrix}; \qquad M_z = \begin{pmatrix} cos\varphi & \rho sin\varphi & 0 \\ -\frac{1}{\rho}sin\varphi & cos\varphi & 0 \\ 0 & 0 & 1 \end{pmatrix} \tag{2.24}$$

Note that M_x is exact for $\delta = \varphi/2$ while $\varphi \ll 1$ has been used for M_z only. We conclude that in a rectangular magnet the weak horizontal focusing of a sector magnet is exactly compensated by the defocusing at the entrance and exit face. The magnet acquires, however, a weak vertical focusing of the same strength.

2.9 Quadrupole magnets

In a quadrupole magnet, $\frac{1}{R} = 0$. The focusing quadrupole can be described with the following matrix.

$$R_{QF} = \begin{pmatrix} \cos\sqrt{k}L & \frac{1}{\sqrt{k}}\sin\sqrt{k}L & 0 \\ -\sqrt{k}\sin\sqrt{k}L & \cos\sqrt{k}L & 0 \\ 0 & 0 & 1 \end{pmatrix} \tag{2.25}$$

As can be seen from equation (2.24), the transfer matrix results in the other level in each case by k being replaced by $-k$. That is, one focusing quadrupole magnet is defocussing in the other plane. The transfer matrix of the defocusing quadrupole can be written as

$$R_{QD} = \begin{pmatrix} \cosh\sqrt{k}L & \frac{1}{\sqrt{k}}\sinh\sqrt{k}L & 0 \\ -\sqrt{k}\sinh\sqrt{k}L & \cosh\sqrt{k}L & 0 \\ 0 & 0 & 1 \end{pmatrix} \tag{2.26}$$

In many cases, the focal length f of the quadrupole is much larger than the length of the magnet $l \ll \frac{1}{kl} = f$. Then the transfermartins in the "thin lens" approximation become easier

$$R_{QF} = \begin{pmatrix} 1 & 0 & 0 \\ -\frac{1}{f} & 1 & 0 \\ 0 & 0 & 1 \end{pmatrix} \quad \text{and} \quad R_{QD} = \begin{pmatrix} 1 & 0 & 0 \\ \frac{1}{f} & 1 & 0 \\ 0 & 0 & 1 \end{pmatrix} \tag{2.27}$$

However, these matrices describe a magnet of length 0. Therefore, one has to consider the geometric length by multiplying two drift distances with the length $l\,/\,2$. The correct transfer matrices close to "thin lenses" are thus.

$$R_{QF} = \begin{pmatrix} 1-\frac{l}{2f} & l-\frac{l^2}{4f} & 0 \\ -\frac{1}{f} & 1-\frac{l}{2f} & 0 \\ 0 & 0 & 1 \end{pmatrix} \quad \text{and} \quad R_{QD} = \begin{pmatrix} 1+\frac{l}{2f} & l+\frac{l^2}{4f} & 0 \\ \frac{1}{f} & 1+\frac{l}{2f} & 0 \\ 0 & 0 & 1 \end{pmatrix} \tag{2.28}$$

2.10 Solenoid magnets

The transfer matrices of a solenoid magnet can not be divided into vertical and horizontal matrices, because there is a coupling between the two transverse planes in the solenoid magnet. The matrices given here transform the vector (x, x', y, y').

The transfer matrix upon entering the solenoids is given by [3]

$$M_{sol,A} = \begin{pmatrix} 1 & 0 & 0 & 0 \\ 0 & 1 & \frac{eB}{2p} & 0 \\ 0 & 0 & 1 & 0 \\ -eB/2p & 0 & 0 & 1 \end{pmatrix} \tag{2.29}$$

The transfer matrix within the solenoid magnet is given by

$$M_{sol,A} = \begin{pmatrix} 1 & \frac{p}{eB}\sin\theta & 0 & \frac{p}{eB}(1-\cos\theta) \\ 0 & \cos\theta & 0 & \sin\theta \\ 0 & -\frac{p}{eB}(1-\cos\theta) & 1 & \frac{p}{eB}\sin\theta \\ -\sin\theta & 0 & 0 & \cos\theta \end{pmatrix} \tag{2.30}$$

with the angle $\theta = 2L \cdot \frac{eB}{2p}$, where L denotes the length of the solenoid magnet. The transfer matrix at the output of the solenoid magnet

$$M_{sol,A} = \begin{pmatrix} 1 & 0 & 0 & 0 \\ 0 & 1 & -\frac{eB}{2p} & 0 \\ 0 & 0 & 1 & 0 \\ eB/2p & 0 & 0 & 1 \end{pmatrix} \tag{2.31}$$

The transfer matrix for the complete solenoid magnet is calculated as the product of the three matrices, $M_{ges} = M_{sol,E} \cdot M_{sol,M} \cdot M_{sol,A}$. In the approximation for "thin lenses", the transfer matrix simplifies to [3]

$$M_{sol,A} = \begin{pmatrix} 1 & 0 & 0 & 0 \\ -1/f & 1 & 0 & 0 \\ 0 & 0 & 1 & 0 \\ 0 & 0 & -1/f & 1 \end{pmatrix} \tag{2.32}$$

with the focal length $f = \left(\frac{eB}{2p}\right)^2 L$.

2.11 Thin-lens approximation

In many practical cases, the focal length f of the quadrupole magnet will be much larger than the length of the lens:

$f = \frac{1}{kl} \gg l$

Then the transfer matrices can be approximated by

$$M_x = \begin{pmatrix} 1 & 0 & 0 \\ \frac{1}{f} & 1 & 0 \\ 0 & 0 & 1 \end{pmatrix} \tag{2.33}$$

$$M_Z = \begin{pmatrix} 1 & 0 & 0 \\ -\frac{1}{f} & 1 & 0 \\ 0 & 0 & 1 \end{pmatrix} \tag{2.34}$$

Note that these matrices describe a lens of zero length, i.e. they are derived from Eqs. (3.14) using $l \to 0$ while keeping $k \cdot l = const$. The true length l of the lens has to be recovered by two drift spaces $l/2$ on either side, e.g.

$$M_z = \begin{pmatrix} 1 & \frac{l}{2} & 0 \\ 0 & 1 & 0 \\ 0 & 0 & 1 \end{pmatrix} \begin{pmatrix} 1 & 0 & 0 \\ -\frac{1}{f} & 1 & 0 \\ 0 & 0 & 1 \end{pmatrix} \begin{pmatrix} 1 & \frac{l}{2} & 0 \\ 0 & 1 & 0 \\ 0 & 0 & 1 \end{pmatrix} = \begin{pmatrix} 1 - \frac{l}{2f} & l - \frac{l^2}{4f} & 0 \\ -\frac{1}{f} & 1 - \frac{l}{2f} & 0 \\ 0 & 0 & 1 \end{pmatrix} \tag{2.35}$$

One might ask why the approximation has not been made by expanding$sin\varphi$, $\cos\varphi$, etc. in Taylor series and neglecting higher powers of φ. However, terminating the Taylor series at some power, results in a transfer matrix whose determinant is not unity. For instance, in third order we obtain

$$M_z = \begin{pmatrix} 1-\frac{l}{2f} & l-\frac{l^2}{6f} & 0 \\ -\frac{1}{f} & 1-\frac{l}{2f} & 0 \\ 0 & 0 & 1 \end{pmatrix} \tag{2.36}$$

which **does not fulfil** $det\ \boldsymbol{M} = 1$. It can be shown that this would violate Liouville's Theorem of phase-space conservation.

For accelerators in the TeV range, where $1/\rho^2 << |k| << 1/l^2$, the thin-lens approximation is excellent for the matrix description of the entire accelerator.

2.12 Quadrupole doublet

The transformation matrix of a system of dipoles, quadrupoles and drift spaces is obtained by multiplying the matrices of each element in the correct order. An important example is a quadrupole doublet consisting of a focusing quadrupole, a drift space and a defocusing quadrupole. **Figure 2.8** shows two trajectories (1,2) suggesting a tendency of both horizontal and vertical focusing in this kind of arrangement.

Figure 2.8: A quadrupole doublet consisting of a horizontally and a vertically focusing quadrupole magnet. Trajectories 1 and 2 suggest that there is a tendency of simultaneous focusing in both the horizontal and vertical directions.

The focusing action arises because trajectories entering parallel to the axis have a larger amplitude in the focusing than in the defocusing lens. Quadrupole doublets are indeed the simplest means of high energy beam focusing and imaging. We shall now derive the conditions for *simultaneous imaging in both* horizontal and vertical planes, treating the quadrupoles in the thin-lens approximation and assuming $f_{foc} = f_{defoc} = f$ for simplicity. The horizontal transfer matrix of the doublet is (for meaning of symbols see Fig. 21).

$$M_{doub,x} = \begin{pmatrix} 1 & 0 & 0 \\ \frac{1}{f} & 1 & 0 \\ 0 & 0 & 1 \end{pmatrix} \begin{pmatrix} 1 & l & 0 \\ 0 & 1 & 0 \\ 0 & 0 & 1 \end{pmatrix} \begin{pmatrix} 1 & 0 & 0 \\ -\frac{1}{f} & 1 & 0 \\ 0 & 0 & 1 \end{pmatrix} = \begin{pmatrix} 1-\frac{l}{f} & l & 0 \\ -\frac{l}{f^2} & 1+\frac{l}{f} & 0 \\ 0 & 0 & 1 \end{pmatrix} \tag{2.37}$$

The vertical transfer matrix is obtained if f is replaced by $-f$:

$$M_{doub,z} = \begin{pmatrix} 1+\frac{l}{f} & l & 0 \\ -\frac{l}{f^2} & 1-\frac{l}{f} & 0 \\ 0 & 0 & 1 \end{pmatrix} \tag{2.38}$$

The matrix element $M_{21} = C' = -\ l/f^2$ is called the overall refractive power of the system and it is seen to be focusing in both planes. Somewhat sloppily one could say that a

beam coming from infinity (i.e. all particles perfectly parallel to the s-axis, $x_0' = 0$) will be focused in both planes, as indicated by trajectories 1 and 2 in **Fig. 2.8**. The effective focal length f_{doub} for these particles is

$$f_{doub} = \frac{f^2}{l}$$

3. Magnets field measurement methods

3.1 Choice of measurement method

The choice of the measurement method depends on several factors. The field strength, homogeneity and variation in time, as well as the required accuracy all need to be considered. Also the number of magnets to be measured can determine the method and equipment to be deployed. As a guide, **Fig. 3.1** shows the accuracy which can be obtained in an absolute measurement as a function of the field level, using commercially available equipment. An order of magnitude may be gained by improving the methods in the laboratory.

The rotating coil method is a general and accurate method to measure the field quality of magnets: integrated field value, higher order multipoles, and magnetic axis. Recent instrumentation and acquisition systems allow high bandwidth and fully automated measurements. This method is the obvious choice for normal quadrupole magnets, and for superconducting magnets having circular apertures and where beam optics considerations require unprecedented precision in the field quality.

These various methods complement each other. They are complemented by the use of Hall plates for local measurements and of NMR based instruments for high absolute accuracy and calibration. A cross-check between these various methods should be used whenever possible to ascertain precision in magnet measurements.

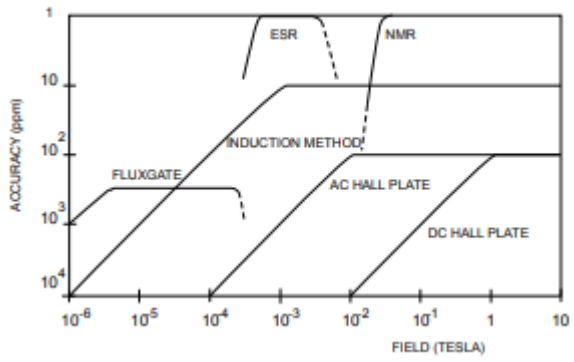

Fig. 3.1 Measurement methods: accuracies and ranges

3.2 The Hall generator method

E.H. Hall discovered in 1879 that a very thin metal strip immersed in a transverse magnetic field and carrying a current developed a voltage mutually at right angles to the

current and field that opposed the Lorentz force on the electrons. In 1910 the first magnetic measurements were performed using this effect. It is a simple and fast measurement method, providing relatively good accuracy, and therefore the most commonly used in large-scale field mapping. The accuracy can be improved at the expense of measurement speed.

The Hall generator provides an instant measurement, uses very simple electronic measurement equipment and offers a compact probe, suitable for point measurements. A large selection of this type of gaussmeter is now commercially available. The probes can be mounted on relatively light positioning gear. Considerable measurement time may be gained by mounting Hall generators in modular multi-probe arrays and applying multiplexed voltage measurement. Also simultaneous measurements in two or three dimensions may be carried out with suitable probe arrays. The wide dynamic range and the possibility of static operation are other attractive features.

However, several factors set limits on the obtainable accuracy. The most serious is the temperature coefficient of the Hall voltage. Temperature stabilization is usually employed in order to overcome this problem but increases the size of the probe assembly. The temperature coefficient may also be taken into account in the probe calibration by monitoring the temperature during measurements. It depends, however, also on the level of the magnetic field, so relatively complex calibration tables are needed. Another complication can be that of the planar Hall effect, which makes the measurement of a weak field component normal to the plane of the Hall generator problematic if a strong field component is present parallel to this plane. This effect limits the use in fields of unknown geometry and in particular its use for determination of field geometry.

Last but not least is the problem of the nonlinearity of the calibration curve, since the Hall coefficient is a function of the field level. The Hall generator of the cruciform type shows a better linearity and has a smaller active surface than the classical rectangular generator. Its magnetic center is, therefore, better defined, so it is particularly well suited for measurements in strongly inhomogeneous fields. Special types, which have a smaller temperature dependence, are available on the market, but these show a lower sensitivity.

The measurement of the Hall voltage sets a limit of about 20 μT on the sensitivity and resolution of the measurement, if conventional DC excitation is applied to the probe. This is mainly caused by thermally induced voltages in cables and connectors. The sensitivity can be improved considerably by application of a.c. excitation. A good accuracy at low fields can then be achieved by employing synchronous detection techniques for the measurement of the Hall voltage. Special Hall generators for use at cryogenic temperatures are also commercially available. Although they show a very low temperature coefficient, they unfortunately reveal an additional problem at low temperatures. The so-called "Shubnikov-de Haas effect" shows up as a field dependent oscillatory effect of the Hall coefficient which may amount to about

one per cent at high fields, depending on the type of semiconductor used for the Hall generator. This adds a serious complication to the calibration. The problem may be solved by locating the Hall generator in a heated anticryostat. Altogether, the Hall generator has proved very useful for measurements at low temperature.

Hall generators are usually calibrated in a magnet in which the field is measured simultaneously using the nuclear magnetic resonance technique. The calibration curve is most commonly represented in the form of a polynomial of relatively high order (7 or 9) fitted to a sufficiently large number of calibration points. This representation has the advantage of a simple computation of the magnetic induction from a relatively small table of coefficients.

A physically better representation is the use of a piecewise cubic interpolation through a sufficient number of calibration points which were measured with high precision. This can be done in the form of a simple Lagrange interpolation or even better with a cubic spline function. The advantage of the spline function comes from its minimum curvature and its "best approximation" properties. The function adjusts itself easily to nonanalytic functions and is very well suited to interpolation from tables of experimental data. The function is defined as a piecewise polynomial of third degree passing through the calibration points such that the derivative of the function is continuous at these points. Very efficient algorithms can be found in the literature. The calculation of the polynomial coefficients may be somewhat time-consuming but need only be done once at calibration time. The coefficients (typically about 60 for the bipolar calibration of a cruciform Hall generator) can be easily stored in a microprocessor device and the subsequent field calculations are very fast. The quality of the calibration function can be verified from field values measured between the calibration points. A well designed Hall-probe assembly can be calibrated to a long term accuracy of 100 *ppm*. The stability may be considerably improved by powering the Hall generator permanently and by keeping its temperature constant.

3.3 Rotating coil method

The harmonic or rotating coil technique gives high resolution and measures in one coil revolution all relevant parameters of any accelerator magnet. Both theoretical and experimental developments allow one to confidently design sophisticated instruments measuring with high bandwidth and precision the full harmonic content of a magnet. It is the best method for measuring higher order multipoles within a well-established theoretical frame, in particular of superconducting and quadrupole magnets having circular apertures.

3.3.1 Description of the harmonic coil method

A perfect dipole magnet gives a constant vertical field everywhere in the useful aperture. The flux enclosed by the simple coil described in Fig. 3.2 will be, considering an infinitely thin winding,

$$\Psi(\theta) = N_t \cdot L \cdot \int_{R_1}^{R_2} B_1 \cdot \cos\theta \cdot dR \tag{3.1}$$

N_t and L are respectively the number of turns and length of the measuring coil. The coil is supposed to be shorter than the magnet. The coil's effective surface can be calibrated independently and is given by

$$\Sigma_{coil} = N_t \cdot L \cdot \int_{R_1}^{R_2} dR = N_t \cdot L \cdot (R_2 - R_1) \tag{3.2}$$

The use of a voltage integrator connected to the measuring coil makes it possible to eliminate the time coordinate in the induction law of Faraday. The voltage integrator read as a function of the angle gives the flux directly from the zero angle where it is reset. The constant of integration is irrelevant for this method.

Fig. 3.2: 2D representation of the flux seen by a simple coil rotating in a dipole field

The units of Eq. (3.1) are

$$\Psi = \text{volt} \cdot \text{sec} = tesla \cdot m^2 = weber \tag{3.3}$$

It is important to realize that the harmonic coil method does not make use of the voltage integrated over a given time, but rather over a given angular interval. The advantage of using a voltage integrator that can be externally triggered is that it eliminates to the first order the problem of a constant speed of rotation. A real system in fact measures differences of fluxes between two incremental angular positions. The angular encoder mounted on one coil end is a fundamental piece of equipment. The integrator is triggered by this encoder and collects incremental fluxes $\delta\Psi_k$, and the left part of Eq. (3.1) becomes

$$\Psi(\theta_i) - \Psi(\theta_0) = \sum_{k=1}^{i} \delta\Psi_k \tag{3.4}$$

with

$$\delta\Psi_k = \Psi(\theta_k) - \Psi(\theta_{k-1}) \tag{3.5}$$

3.3.2 Measuring the multipoles by rotating coils

The power of the harmonic coil method is its ability to measure any type of 2D magnetic field. It can be demonstrated that a rotating coil measures the 2D field integrated over its length as long as the field component parallel to the rotation axis is zero on the two coil ends. The complex equation to best describe this 2D field is

$$B(x + i \cdot y) = B_y(z) + i \cdot B_x(z) = \sum_{n=1}^{\infty} C_n \cdot \left(\frac{z}{R_r}\right)^{n-1} \tag{3.6}$$

The components $C_n = B_n + iA_n$ are the normal and skew multipoles of the field. By definition for accelerator magnets, the normal components indicate a vertical field in the horizontal plane whilst the 'skew' terms apply for an horizontal field. The C_n are in tesla at the reference radius R_r . **Figure 3.3** shows the field lines for normal and skew dipoles (C_1) and quadrupoles (C_2).

The field quality is usually described as errors relative to the main field component B_M ($M = 1$ for a dipole, $M = 2$ for a quadrupole) at the reference radius R_r. These errors are called 'units' and are given by

$$c_n = b_n + i \cdot a_n = 10^4 \frac{C_n}{B_M} \tag{3.7}$$

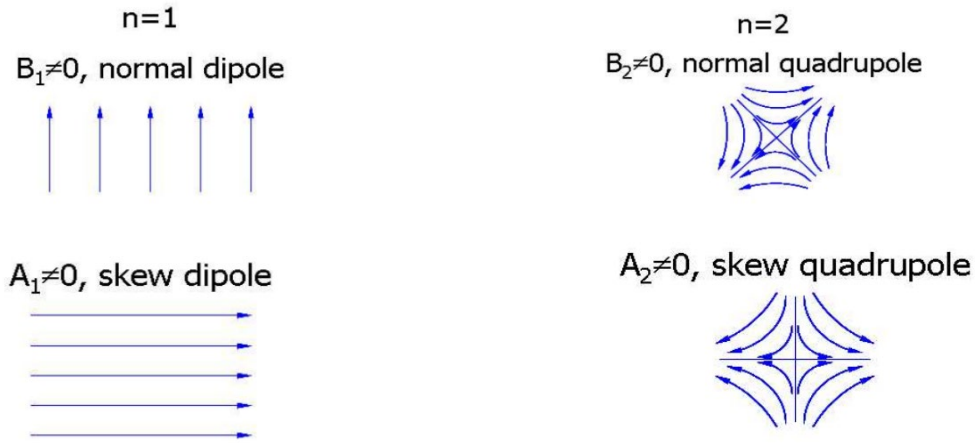

Fig. 3.3: Field lines of normal and skew dipole and quadrupole magnets

The reference radius R_r is an important concept for accelerator magnets having apertures much smaller than one metre. R_r corresponds in practice to

- the useful aperture for the beam,
- 2/3 of the yoke aperture in resistive magnets,
- 2/3 of the coil aperture in superconducting magnets,
- the radius where the multipoles relative to the main field, thec_n in **Eq. (3.7)**, have the same order of magnitude in a real magnet.

It is important to carefully choose this reference radius at the beginning of a project. It will intervene in the discussions between all actors involved: beam optic physicists, magnet designers, measurement crew, and data analysis teams.

The voltage integrated over a simple rotating coil described in **Fig. 3.2** and rotating in any 2D field will therefore be determined by the time derivative of

$$\Psi(z) = N_t \cdot L \cdot Re \int_{R_1}^{R_2} B(z) \cdot dz \tag{3.8}$$

Since the coil rotates

$$z = x + i \cdot y = R \cdot e^{i\theta(t)} \tag{3.9}$$

and by applying Eq. (3.6) and integrating it over dR

$$\Psi(\theta = \omega \cdot t) = Re\left(\sum_{n=1}^{\infty} N_t \cdot L \cdot \frac{R_2^n - R_1^n}{n \cdot R_r^{n-1}} \cdot C_n \cdot e^{in\theta}\right) \quad (3.10)$$

This allows a formal separation between what belongs to

- the measured field components C_n,
- the time dependence of the signal $e^{in\theta(t)}$,
- the coil sensitivity factor K_n defined as

$$K_n = N_t \cdot L \cdot \frac{R_2^n - R_1^n}{n \cdot R_r^{n-1}} \quad (3.11)$$

The K_n are calculated once for each measuring coil used. They can be complex numbers in the case of tangential coils, or coils not perfectly aligned radially. These calculations are substantial if the wires can no longer be considered point-like. Their values can be improved by individual calibrations.

The multipoles of the field are directly given by the Fourier analysis coefficients Ψ_n of the integrated voltage over a coil turn $\Psi(\theta)$:

$$\Psi_n = K_n \cdot C_n = K_n \cdot (B_n + iA_n) \quad (3.12)$$

3.3.3 Errors associated with the harmonic coil method

Mechanical or electronic imperfections mainly degrade the measurement of the 'higher order' multipoles, i.e., those with harmonic numbers higher than the magnet multipole order. The three main error sources will be studied in detail:

- voltage integrator offset coupled with irregular rotation rate of the coil,
- error in the coil angle measurement due either to the angular encoder or to torsions of the coil shaft during rotation,
- instability or movement of the rotation axis of the coil shaft due to gravity, bearings quality, or vibrations.

Schemes of compensation coil arrays, connected in opposition, have been developed to remove the signal coming from the magnet main multipole thus allowing the increase of the amplification factor at the input of the integrator. More importantly, these compensation coil assemblies remove nonlinear coupling coming from the main harmonic and degrading the high-order harmonic measurement.

4. Dipole and quadrupole measurements with compensated rotating coil

4.1 INTRODUCTION

Measurement of the Vector Potential

Consider the flux enclosed by a pair of coils. The voltage excited in a closed loop is proportional to the change in the total magnetic flux. The circuitry for collecting the data from a rotating coil includes an integrator. The digital integrator consists of a voltage to frequency converter and an up-down counter (which counts pulses). The output from the integrator is latched at fixed angular positions, triggered by pulses at equal angular intervals from a shaft encoder. A motor is used to rotate the coil at approximately uniform rotational velocity. The output from the integrator will be a cosine curve with periodicity N, where N is the index of the fundamental magnetic field.

A computer collects the data from the integrator triggered by pulses from the shaft encoder. It also controls the magnet power supply, the motor rotating the coil, and collects the output of a shunt or current transductor which monitors the current from the power supply. The computer archives the raw data, performs a Fourier analysis and reduces the data and tabulates multipole errors, normalized to the fundamental and the phases of the multipole errors.

The multipole errors are typically small compared to the fundamental signal.

$$\frac{B_n}{|B_N|} \leq 1 \times 10^{-3} \text{ at the magnet aperture}$$

Thus, the voltage signal from error multipoles is typically substantially less than $1x10^{-3}$ of the voltage signal from the fundamental field. Therefore, a compensated (or bucked) coil configuration is devised which is insensitive to the fundamental field and measures only the error signals.

The geometry of the typical compensated coil is described in the following **Figure 4.1**:

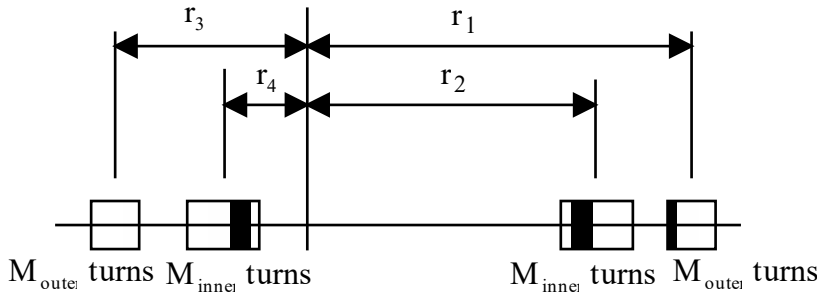

Figure 4.1: The geometry of the typical compensated coil. M_{outer} and M_{inner} are the number of turns of the outer and inner coils, respectively.

4.2 Voltage from the Measurement Coil

The integrated output voltage from a rotating coil in a magnetic field is a function of the magnetic vector potential at the locations of the windings of the coil, the magnet effective length and the number of turns in the measurement coil. In the following discussion, the outer coils are located at radii r_1 and r_3 and sweep the field at complex coordinates z_1 and z_3. The inner coils are located at radii r_2 and r_4 and sweep the field at complex coordinates z_2 and z_4.

4.2. Outer Coil

$$\Phi_{outer} = Integrated\ Voltage = M_{outer}L_{eff}\,\Delta A = M_{outer}L_{eff}Re[F(z_1) - F(z_3)]$$

$$F(z) = \sum C_n z^n = \sum |C_n|\, e^{i\psi_n} r^n e^{in\theta} = \sum |C_n| r^n e^{i(n\theta+\psi_n)}$$

$$A = Re\ F(z) = Re\left[\sum |C_n| r^n e^{i(n\theta+\psi_n)}\right] = \sum |C_n| r^n \cos(n\theta + \psi_n)$$

Substituting

$$\Phi_{outer} = M_{outer}L_{eff}Re[F(z_1) - F(z_3)] = M_{outer}L_{eff}\sum |C_n|(r_1^n - r_3^n)\cos(n\theta + \psi_n)$$

For each term in the expansion;

$$\Phi_{n-outer} = M_{outer}L_{eff}|C_n|(r_1^n - r_3^n)\cos(n\theta + \psi_n)$$

If one takes the Fourier expansion of the measured integrated voltage from the outer coil, the expansion is written;

$$\Phi = \frac{a_0}{2} + \sum_{n=1}^{\infty} a_n \cos n\theta + b_n \sin n\theta$$

$$\Phi_n = a_n \cos n\theta + b_n \sin n\theta$$

$$|\Phi_n| = \sqrt{a_n^2 + b_n^2}$$

But $\Phi_{n-outer} = M_{outer}L_{eff}|C_n|(r_1^n - r_3^n)\cos(n\theta + \psi_n)$

$\cos(n\theta + \psi_n) = \cos n\theta \cos\psi_n - \sin n\theta \sin\psi_n.$

Substituting;

$$\Phi_{n-outer} = M_{outer}L_{eff}|C_n|(r_1^n - r_3^n)(\cos n\theta \cos\psi_n - \sin n\theta \sin\psi_n)$$

From the Fourier analyzed

$$\Phi_n = a_n \cos n\theta + b_n \sin n\theta$$

Equating the coefficients in the Fourier analysis of the integrator output.

$a_n = M_{outer}L_{eff}|C_n|(r_1^n - r_3^n)\cos\psi_n$

$b_n = M_{outer}L_{eff}|C_n|(r_1^n - r_3^n)\sin\psi_n$

$$\tan\psi_n = \frac{\sin\psi_n}{\cos\psi_n} = \frac{-\dfrac{b_n}{M_{outer}L_{eff}|C_n|(r_1^n - r_3^n)}}{\dfrac{a_n}{M_{outer}L_{eff}|C_n|(r_1^n - r_3^n)}} = -\frac{b_n}{a_n}$$

$$\psi_n = \arctan(-b_n/a_n)$$

$$| \Phi_{n-outer} | = \sqrt{a_n^2 + b_n^2} = M_{outer} L_{eff} |C_n| (r_1^n - r_3^n)$$

4.2.3 The Fundamental Field

Measurements of the fundamental field (n=N) are made using the **outer coil**.

$\Phi_N = M_{outer} L_{eff} |C_n| (r_1^N - r_3^N)$

We define the following terms.

$\beta_1 \equiv \frac{r_3}{r_1}$ where β_1 is a positive number.

$$S_n \equiv (1 - (-\beta_1)^N)$$

$$|\Phi_N| = M_{outer} L_{eff} |C_n| (r_1^N - r_3^N) = M_{outer} L_{eff} |C_n| (r_1^N - r_3^N)$$

$$= M_{outer} L_{eff} |C_n| r_1^N (1 - (-\beta_1)^N) = M_{outer} L_{eff} |C_n| r_1^N S_n$$

$$|C_N| = \frac{|\Phi_N|}{M_{outer} L_{eff}\, r_1^N S_n}$$

$$|H_N|_{r_1} L_{eff} = N\, |C_N| r_1^{N-1} L_{eff}$$

$$\boxed{|H_N|_{r_1} L_{eff} = \frac{N |\Phi_N|}{r_1 M_{outer} S_n}}$$

We check the units.

$$|H_N|_{r_1} L_{eff} = Tm = \frac{W}{m^2} m = \frac{Vsec.}{m}$$

$$\frac{N |\Phi_N|}{r_1 M_{outer} S_n} = \frac{Vsec.}{m}$$

For the magnets which are most usually measured (the dipole, quadrupole and sextupole);

$$\boxed{S_1 = 1 + \beta_1; \quad S_2 = 1 - (-\beta_1)^2; \quad S_3 = 1 - (-\beta_1)^3}$$

4.2.4 Quadrupole Measurement Coil

For a quadrupole coil, it is desirable to make s_2 and $s_1 = 0$.

$$s_2 = \{1 - (-\beta_1)^2 - \mu\rho^2 (1 - (-\beta_2)^2)\} = 1 - \beta_1^2 - \mu\rho^2 (1 - \beta_2^2) = 0$$

$$s_1 = \{1 - (-\beta_1) - \mu\rho(1 - (-\beta_2))\} = 1 + \beta_1 - \mu\rho(1 + \beta_2) = 0$$

The "classical" geometry which satisfies these constraints has the following parameters; $\beta_1 = 0.5;\ \beta_2 = 0.2;\ \rho = 0.625;\ \mu = 2$

The balance of the bucked (i.e. compensated) sensitivities are computed and graphed.

$$s_n = \{1 - (-\beta_1)^n - \mu\rho^n (1 - (-\beta_2)^n)\}$$

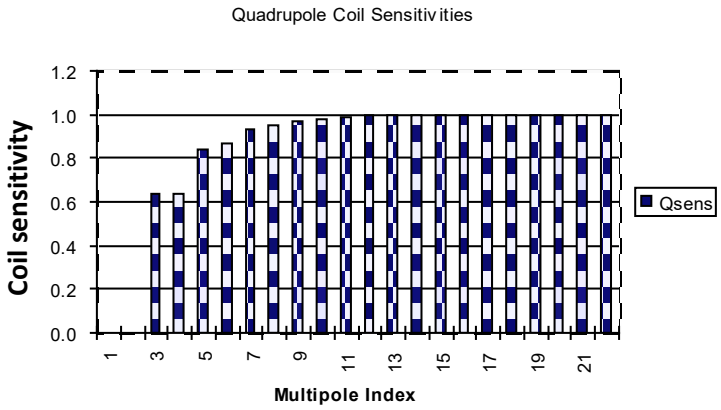

Figure 4.3: Quadrupole coil sensitivities with respect to the multipole content

This coil configuration can also be used to measure a dipole magnet as shown in **Figure 4.3**. Since the coil has no quadrupole sensitivity, a quadrupole error must be evaluated using the "uncompensated" configuration. Since a quadrupole multipole is NOT an allowed multipole for a symmetric dipole magnet, this does not usually present a serious problem. However, if the dipole design constraints requires that the symmetry conditions be violated (e.g. a "C" shaped dipole), the evaluation of a small quadrupole error may be marginal.

One needs to design and fabricate the coil such that the electrical signal obtained from the integrator is sufficiently large for the sensitivity of the instrument. The level of electrical noise in a system is of the order of a few μ *Volts*. Thus, in order to keep the signal above the μ *Volt* range, the measurement coils are wound with many turns (typically > 100).

The Normalized Multipole Error Spectrum

The following figure illustrates a typical "compensated" signal from an integrator. A drift component continues to exist. Also, although the signals from the "higher frequency" signals can be easily detected, the signal is still dominated by the fundamental signal. This is because the desired coil geometry cannot be exactly fabricated and some fundamental signal continues to exist.

A "figure of merit", defined as the bucking ratio, is typically computed as part of the reduced data. This is the ratio of the electrical signal from the fundamental field from the uncompensated and compensated configuration and describes how closely the measurement coil was built to its specified design. A higher value for this bucking ratio indicates how well the fundamental signal has been reduced.

$$Bucking\ ratio = \frac{|\Phi|_{\mathrm{N-unbucked}}}{|\phi|_{N-bucked}}$$

For a carefully fabricated coil, bucking ratios ≈ 400 can be achieved. This means that for a high quality magnet $\left|\frac{B_n}{B_N}\right| \leq 10^{-3}$, the ratio of the fundamental field to the measured error field is ≈ 2.5. A typical raw data output for a quadrupole is shown in the following **Figure 4.4**. It can be seen that, although the error fields are apparent, the signal is still dominated by the remaining fundamental field with a periodicity of two.

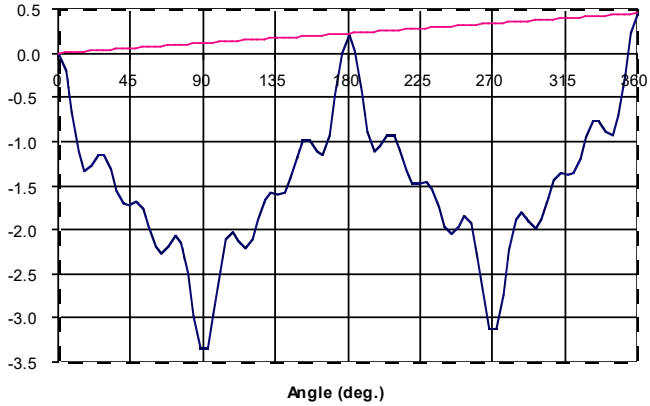

Figure 4.4: A typical raw data output for a quadrupole

After the drift is subtracted from the data, the cosine and sine coefficients of the Fourier expansion for the integrated signal from the "bucked" signal from the integrator can be computed.

$$\phi = \frac{a_0}{2} + \sum_{n=1}^{\infty} a_n \cos n\theta + b_n \sin n\theta$$

$$\phi_n = a_n \cos n\theta + b_n \sin n\theta$$

The expansion can also be expressed in terms of only the cosine terms with a phase angle.

$\phi - \frac{a_0}{2} = \sum_{n=1}^{\infty} |\phi_n| \cos(n\theta + \lambda_n)$ where $|\phi_n| = \sqrt{a_n^2 + b_n^2}$; $\lambda_n = \arctan -\frac{b_n}{a_n}$

For the unbucked configuration; $\boxed{|H_N|_{r_1} L_{eff} = \frac{N|\Phi_N|}{r_1 M_{outer} S_n}}$

For the bucked configuration; $|H_n|_{r_1} L_{eff} = \frac{n|\varphi_{n-bucked}|}{r_1 M_{outer} S_n}$

Thus the measured normalized multipoles are; $\boxed{\left|\frac{H_n}{H_N}\right|_{r_1} = \frac{n|\varphi_n|S_n}{N|\Phi_N|S_n}}$

4.2.5 Dipole Measurements

When the coil is used to measure a dipole magnets, the first error harmonic is the quadrupole field. Since in the bucked configuration, the sensitivity is zero, the quadrupole error harmonic must be measured with the unbucked coil.

$$|H_N|_{r_1} L_{eff} = \frac{N\phi_{Nmagnitude}}{r_1 M_{outer} S_N} => |H_1|_{r_1} L_{eff} = \frac{\phi_{1magnitude}}{r_1 M_{outer} S_1} \quad and \; |H_2|_{r_1} L_{eff} = \frac{2\Phi_{2magnitude}}{r_1 M_{outer} S_2}$$

Therefore, $\left|\frac{H_2}{H_1}\right|_{r_1} = \frac{2S_1}{S_2} \frac{\Phi_{2magnitude}}{\Phi_{1magnitude}}$

5. AREAL magnets

5.1 Introduction

The low energy electron linear accelerator facility AREAL can be considered as the first phase of realization of the synchrotron light source project CANDLE in Armenia. The energy of the electron beam will reach ~50 MeV as the result of the implementation of two 1.5m long accelerator sections. Bending magnets as well as corrector magnets are in use for beam guidance and steering. Beam focusing is realized applying solenoid and several quadrupol magnets in doublet and triplet arrangements. Finally, light with specific properties will be produced through the periodic magnetic structure of an undulator.

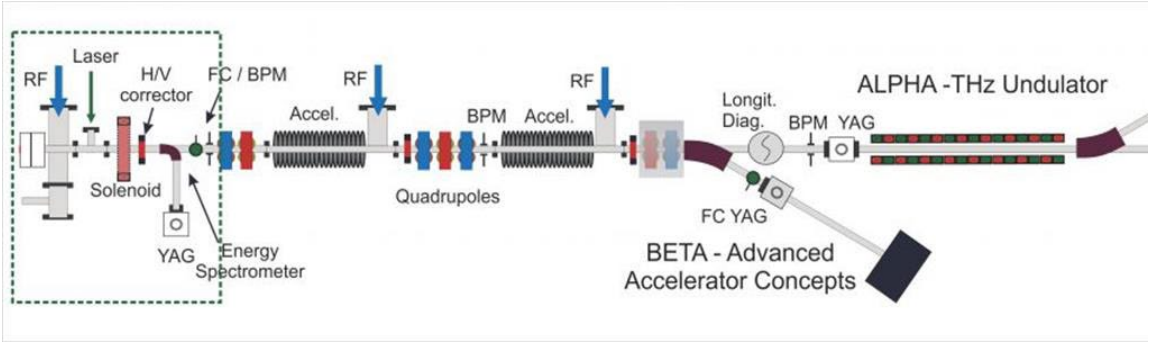

Fig. 5.1: Layout of the low energy electron linear accelerator facility AREAL.

At AREAL, the magnetic field measurements of the magnets and insertion devices is conducted at the Magnetic Measurements Laboratory. It is equipped with two different measurement benches, each one intended for a type of magnetic measurements with different sensors.

Introduction to the accelerator magnets can be found in chapter 2 and Ref. [3].

5.2 Dipole magnet

As a part of the AREAL spectrometer for energy and energy spread measurements, a dipole magnet was designed, fabricated and tested at the CANDLE Synchrotron Research Institute. The energy range of the electron beam achieved just after the RF gun is $2-5\ MeV$. The magnet design and geometry optimization resulted in $12cm \times 12cm$ square poles with a gap of $4cm$ and a yoke size of $8cm \times 6cm$. In the simulations, Steel 1008 material was used with properties close to the steel used in magnet fabrication. The magnet consists of two coils with 500 windings each. In the field measurements a magnet-probe alignment $< 100\mu m$ was reached. **Figure 5.2** presents the mechanical layout of the simulated design and the measured magnetic field distribution along the pole symmetry. Measurements were taken by Hall probes.

Figure 5.3 presents simulated and measured bending field distributions along the electron 90^0 bend trajectory and the measured field in consistency with simulation results.

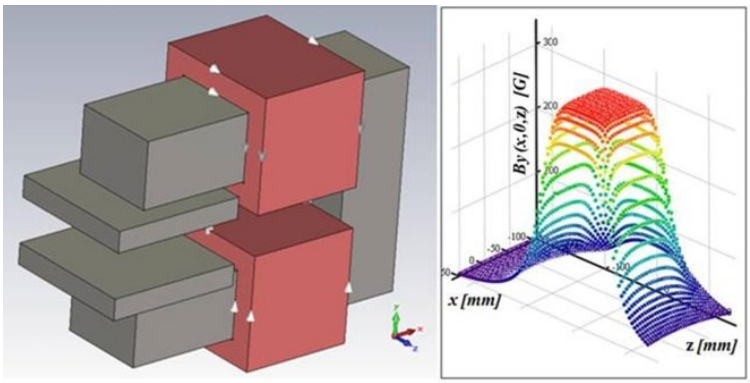

Figure 5.2: AREAL dipole magnet design and measured field map of bending field component.

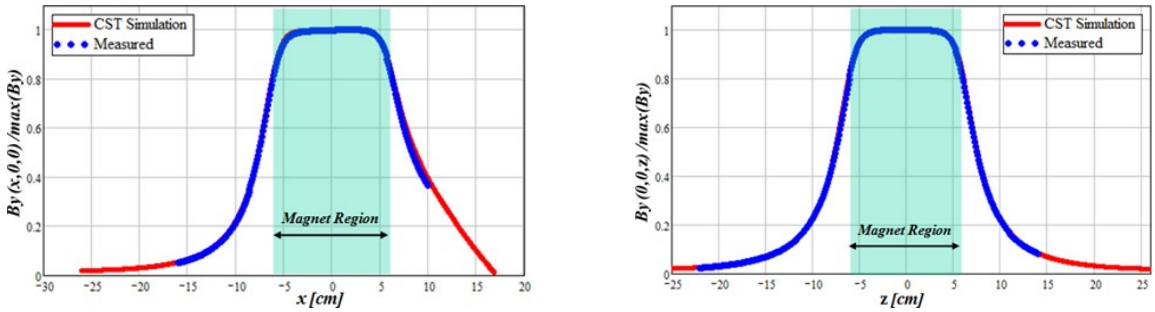

Figure 5.3: Dipole magnet simulated (red) and measured (blue dots) bending field distributions along both horizontal axes in the center.

As it can be seen, the difference between simulated and measured field is less than 2% in the magnet region and increases at far distances from magnet edges. One can also see that the measured field amplitudes are smaller than expected from the simulations which is directly related to fabrication errors and deviations of yoke material properties.

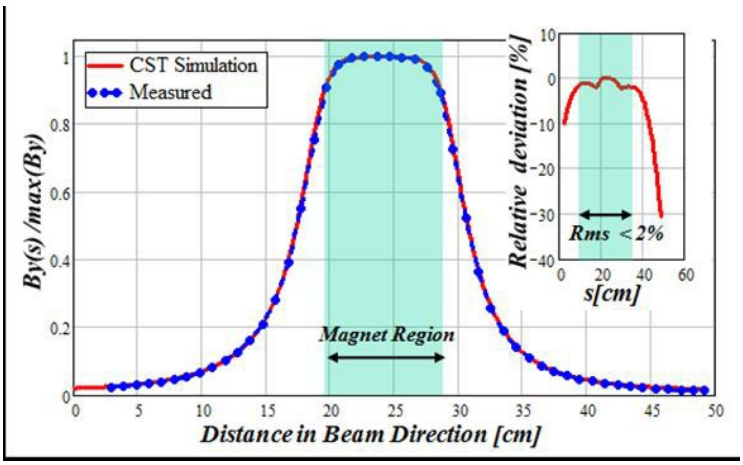

Fig. 5.4: Dipole magnet(left); calculated via CST simulation and measured field (right).

The final analysis of measured and simulated magnetic field results in a relation between the longitudinal momentum P_Z of the electrons and the bending field amplitude B_0 at the pole centre given as $P_Z \left[\frac{MeV}{c}\right] = 0.029 B_0 \, [\, mT \,]$.

To obtain the dispersive properties of this dipole magnet, a particle tracking simulation was performed that includes five particles with different energies with the same initial position (**Fig. 5.5**). In the simulation the particle energies are taken with $dE = 0.25 MeV$ and $dE = 0.5 MeV$ deviations from the design particle energy of 5MeV.

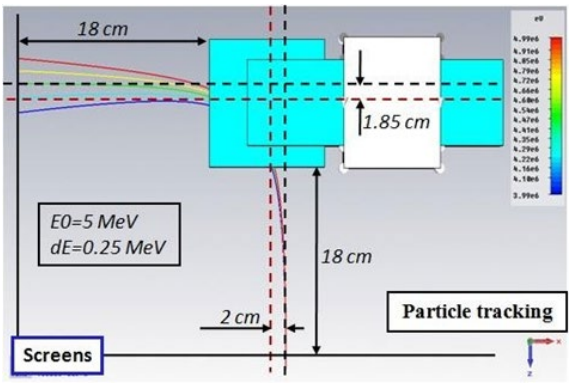

Figure 5.5: Trajectories of the particles with different energies passing the 90° bend dipole. Magnet symmetry axis (red dashed), particle design axis (black dashed) and positions of the screens are presented.

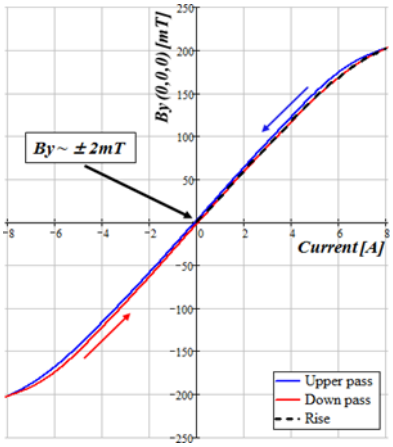

Figure 5.6: Measured hysteresis curve of the dipole magnet.

The final analysis of the transverse phase space at 18cm distance from magnet edge results in a dispersion function of $D = 0.24\, m$ and a dispersion slope $D' = 0.96\, rad$.

Figure 5.6 presents the measured hysteresis curve of the dipole for a maximum coil current of $\sim 8A$. The residual(=remnant) field of the magnet is $\sim 2mT$ that is about 50 times bigger than the measured earth magnetic field of $\sim 0.04mT$. Finally, a magnet degauss procedure was developed from the measurement that is performed in three steps.

5.3 Solenoid magnet

The AREAL solenoid magnet design (**Fig. 5.7**) is modified from a DESY type solenoid. The magnet consists of a single coil with 20 windings and 1 cm thick iron shielding. The magnet length is about 6.4 cm that has cooling passes in the outer surfaces of the iron shield. The magnetic iron cover of the solenoid provides a return path for the magnetic field thus screening effectively the field in the outer space and concentrating it to the inside of the solenoid gap.

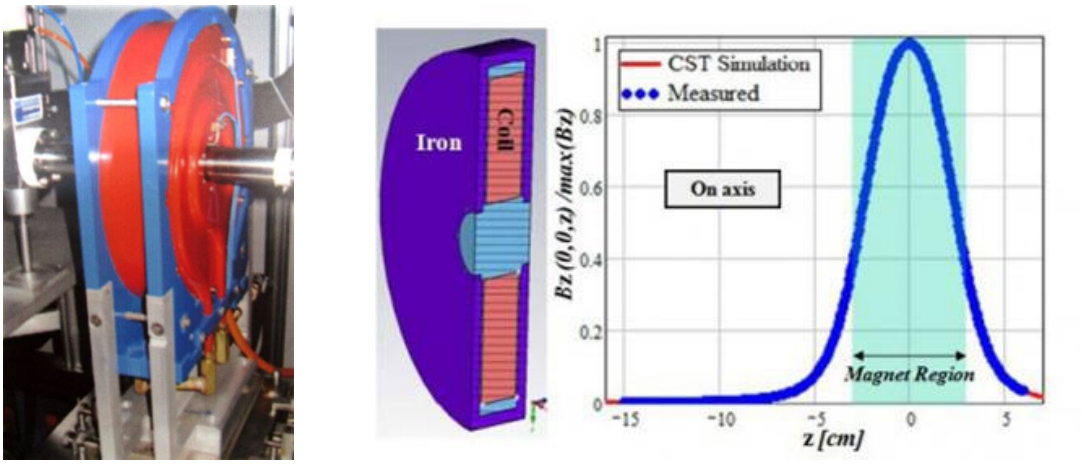

Fig. 5.7: Solenoid magnet and magnet's measured (blue dots) and simulated (red) longitudinal field on axis (right).

During the field measurements the magnet shows stable operation in terms of heating for currents up to 8A that corresponds to the peak magnetic field of ~175mT. **Fig. 5.7** is presenting the measured and simulated longitudinal magnetic field. The difference between measured and simulated fields is less than 2%. During the field measurements, a magnet-probe alignment < 300μm was achieved.

The resulting effective field length of 39.57 mm was obtained that is defined as a normalized integral of B_z^2. According to **Eq. (2.3)**, a focal length of ~85 cm is expected for the 5 MeV electron beam at 8 A solenoid current.

5.4 Corrector magnet

A corrector magnet (**Fig.5.8**) was designed for trajectory steering of electron beams with energies up to 5 MeV. The magnet is iron-free and its coils are optimized to provide a homogeneous steering field region.

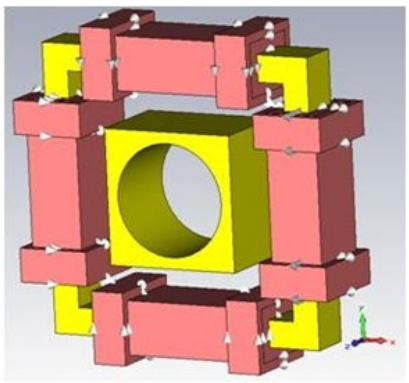

Figure 5.8: Iron-free steering magnet design.

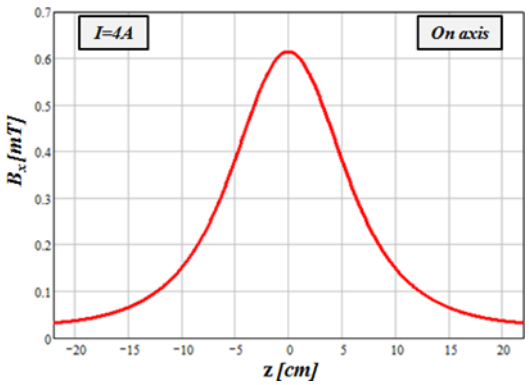

Figure 5.9: The steering magnetic field distribution on the magnet axis in case of excitation of the two coils generating a horizontal steering field.

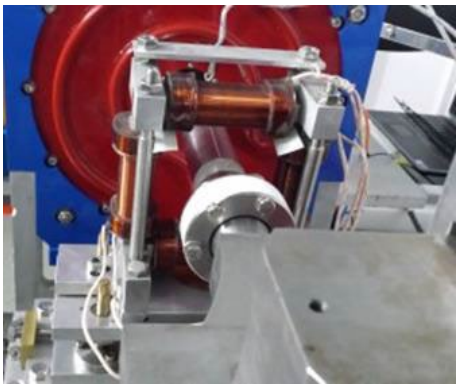

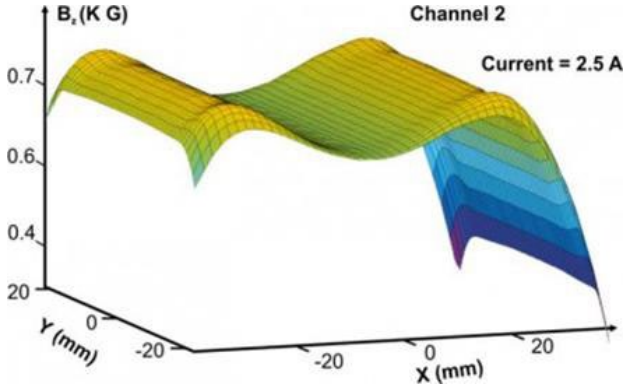

Fig. 5.10: Corrector magnet (left); Field mapping via Hall probe over the transverse plane (right).

The beam trajectory steering in horizontal and vertical planes will be provided by coil doublets that are arranged parallel to each other. The gap of the magnet has 50mm diameter and a maximum current of 4 A is assumed in each coil doublet (**Fig 5.9**). Each coil consists of 480 windings in the center coil and 60 windings in both edge coils. The steering field distribution is presented in **Figure 5.10** which will provide a maximum of ~5.6 $mrad$ integrated transverse kick to the 5MeV electron beam. The effective length of the steering field is 15.2 cm and the maximum field is $B_0 \approx 0.6mT$ at 4A current. The good steering field region is within the transverse circle of radius 8 mm that provides a magnetic field of better than 1% homogeneity. As a drawback, the field has a non-vanishing quadrupole component the integrated effect of which is, in comparison with the dipole component $< 0.6\%$. Finally, one concludes that this iron-free corrector will provide a steering field with accuracy $< 1\%$ within the good field region of 8mm radius.

5.5 Quadrupole magnet doublet for AREAL

A symmetric quadrupole doublet configuration has been chosen to allow varying the beam spot size and its shape on the target. The symmetric quadrupole produces an optimum target beam spot uniformity assuming an axially symmetric input beam.

Table 5.1: Magnets parameters

Doublet length by Iron	165 mm
Magnet length	60 mm
Distance (iron to iron)	45 mm
Distance between centers	0.105 m
Magnet bore diameter	43 mm
Net focal length of system at 5MeV	1.1 m
Field gradient	0.6 T/m
Magnet Inductance	19 mH

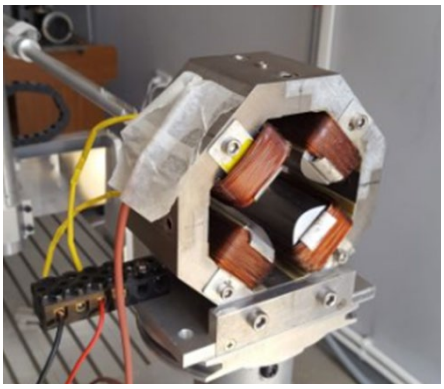

Figure 5.11: Quadrupole magnet at measurement laboratory.

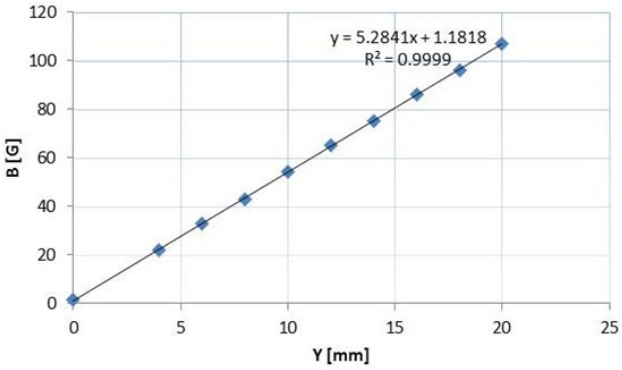

Figure 5.12: Horizontal field mapping via Hall probe over the vertical axis (right).

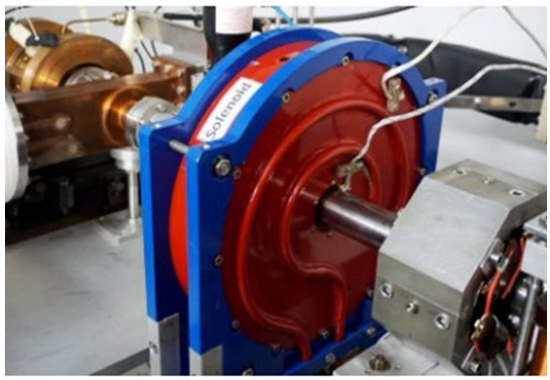

Figure 5.13: The quadrupole magnet is mounted downstream to the solenoid magnet for beam measurements.

6. Magnet measurements

At AREAL, the magnetic field measurements of the magnets and insertion devices is conducted at the Magnetic Measurements Laboratory. It is equipped with two different measurement benches, each one intended for magnetic measurements with different sensors.

Introduction to the accelerator magnets can be found in chapter 2 and in Ref. [3].

6.1 Equipment and tools

The measurements of dipole, solenoid, corrector and quadrupole magnets are important parts of the AREAL electron facility program. The CANDLE diagnostics laboratory has successfully completed the high precision Magnetic Measurement Bench (MMB) that enables one to map the magnetic field with high accuracy. The results of these measurements agree well with the magnet simulations performed by the magnetic field simulation codes POISSON

and CST Microwave Studio. Relying on the measurement data, the magnets are constructed and the AREAL first electron beam was successfully obtained on 20 December 2013.

Figure 6.1: Magnetic Measurement Bench; the maximum movement along the directions is $x = 40cm$, $y = 90cm$, $z = 14cm$, where z is directed along the robotic arm. The minimum step is $10^{-4}cm$.

The Magnetic Measurement Bench is equipped with a robotic arm carrying the magnetic field point sensor, a step motor, a control and a power supply unit [**Fig 6.1**]. It uses a Lake Shore Model 425 gaussmeter and 400 Series axial and transverse pick up Hall Probes as field sensors [http://www.lakeshore.com]. The parameters of the gaussmeter and Hall Probes are given below.

Lake Shore Model 425 gaussmeter parameters:

Field ranges from 350 mG to 350 kG,
DC measurement resolution to 1 part of ±35,000,
Basic DC accuracy of ±0.20%,
DC to 10 kHz AC frequency,
USB interface,
Large liquid crystal display,
Sort function (displays pass/fail message)
Alarm with relay
Standard probe included
Standard and custom probes available

Figure 6.2: Lake Shore Model 425

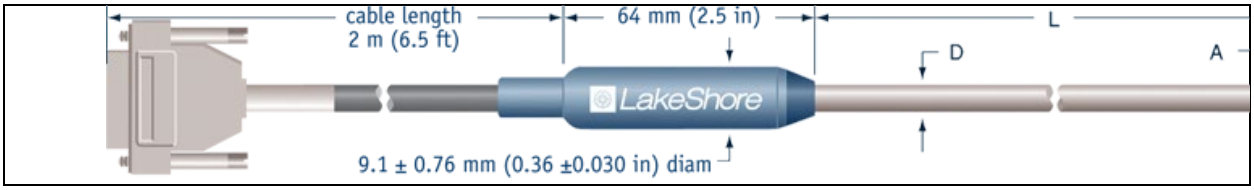

Figure 6.3: Axial Probe

Model	L mm	D mm (in)	A mm (in)	Active area mm (in)	Stem material	Frequency range	Usable full scale ranges	Corrected accuracy (% rdg at 25^{0}C)	Temp coefficient (max) zero	Temp coefficient (max) Calibration	Contains temp sensor
HMNA-1904-VR	4 ± 0.125	0.187 *dia* ± 0.005	0.005 ± 0.003	0.030 *dia*	Fiberglass epoxy	DC to 10 kHz	HSE 35G 350 G, 3.5kG,35kG	$\pm 0.2\%\ to\ 30kG$ and $\pm 0.25\%\ 30\ to\ 35kG$	$0^0C\ to\ 75^0$	$\pm 0.09G/C$	$-0.04\%/C$

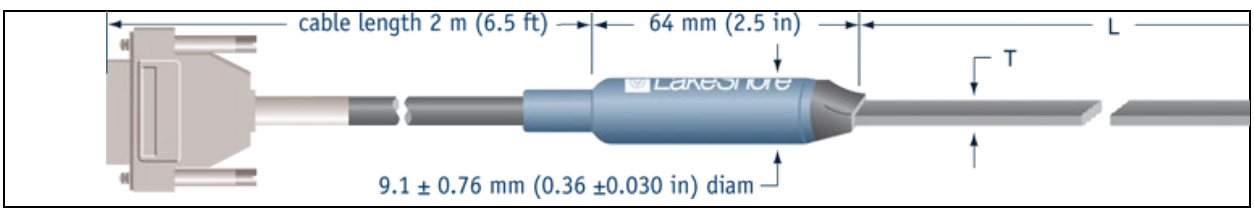

Figure 6.4: Transverse Probe

Model	L mm	T mm (in)	W mm (in)	A mm (in)	Active area (in)	Stem material	Frequency range	Usable full scale ranges	Corrected accuracy (% rdg at 25°C)	Temp coefficient (max) zero	Contains temp sensor
HMMT-6J08-VR	8 ± 0.125	0.061 *max*	0.18 ± 0.005	0.15 ± 0.05	0.04 *dia*	Aluminum	DC to 800 Hz	HSE 35G 350 G, 3.5kG,35kG	$\pm 0.2\%\ to\ 30kG$ and $\pm 0.25\%\ 30\ to\ 35k$	$\pm 0.09G/C$	$-0.04\%/C$

LITERATURE

1. http://candle.am/design_report .
2. http://candle.am/areal/#, B. Grigoryan et al., MOPRI017, IPAC2014, http://jacow.org/ .
3. Rossbach, P. Schmüser, Basic course on accelerator optics, DESY-M-93-02.
4. Tsakanian et al, TUPRO078, Proc. IPAC2014, http://jacow.org/.
5. https://laacg.lanl.gov/ .
6. Jack Tanabe, Magnetic Measurements,USPAS, Houston TX, January, 2001.
7. L. Walckiers Magnetic measurement with coils and wires, https://cds.cern.ch/record/1345967/files/p357.pdf.

PRACTICAL HOURS

Task 1: Calibrate and position the Hall-probe gaussmeter.

Position the transverse Hall-probe on the robotic arm.

Turn on Power Supply unit, Gaussmeter, Step motor and robotic arm controller.

Zero and check the calibration of the gaussmeter. Keep the probe away from the bore area of the magnet while calibrating.

Start Mill program on the computer. Note that, in the context of the program X axis goes through the magnet center, Z is vertical axis and Y is horizontal one.

Task: 2 Quadrupole gradient- and calibration measurement

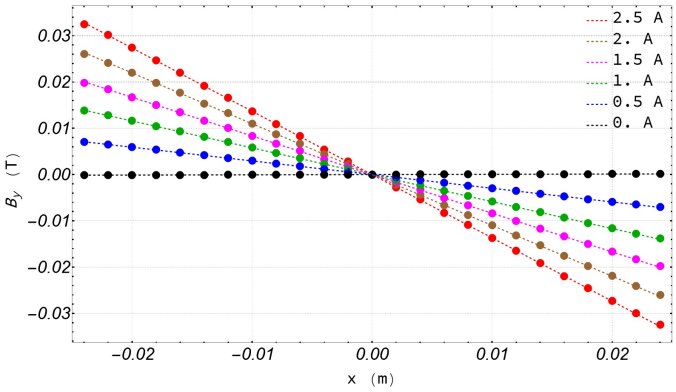

(a) Magnetic field measured at various current settings.

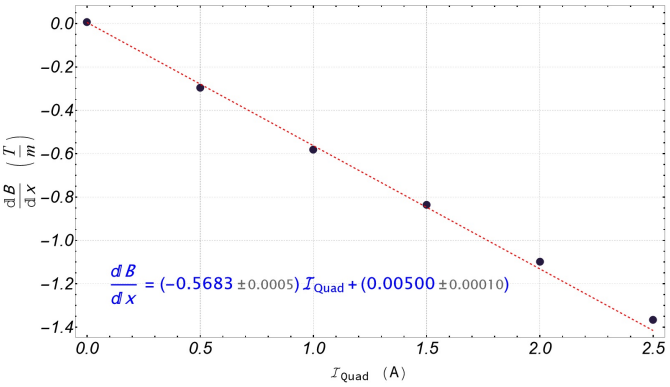

(b) Fitting the gradient calibration function.

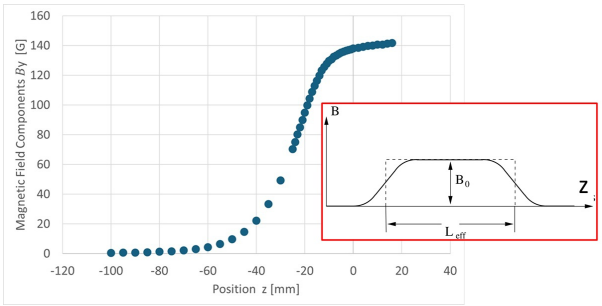

(c) Effective length measurement.

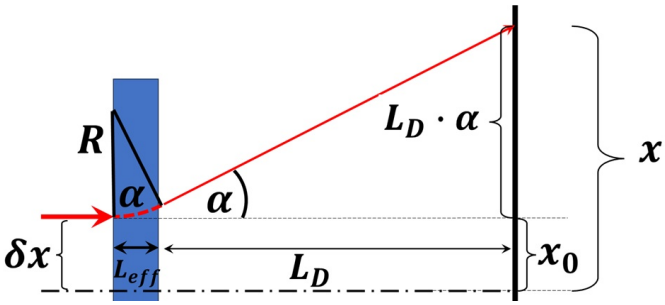

(d) Beam-based alignment.

Figure 1: Examples - measurements and data analysis.

The goal is to determine the quadrupole gradients $g_y(I_Q) = -\frac{\partial B_y}{\partial x}$ and $g_x(I_Q) = -\frac{\partial B_x}{\partial y}$ (see Eq.(2.4)) as a function of the quadrupole current I_Q experimentally. The experiment consists of the following steps:

a) Set the current in the quadrupole to $I_{Q,i}$, where $0\,\text{A} \leq I_{Q,i} \leq 2.5\,\text{A}$,

b) Place the Hall probe at the magnetic center, where the field vanishes, i.e. at the point where $B(x,y) = 0$,

c) Move the probe horizontally in 2 mm steps within the range (-20 mm, 20 mm) from the center. At each horizontal position x measure and record the vertical component of the magnetic field $B_y(x)$,

d) Repeat a)-c) for a different value of $I_{Q,i}$. Ideally the values of $I_{Q,i}$ should be equidistant, separated by a 0.5 A step, so that $I_{Q,i}$={0, 0.5, 1.0, 1.5, 2.0, 2.5} A,

e) Plot the measured data as shown in the example in Fig.1a.

f) For each separate data set $B_y(x)$ (each corresponding to a different $I_{Q,i}$) determine the slope $\frac{\partial B_y}{\partial x}$ by a linear fit $B_y = \frac{\partial B_y}{\partial x}(I_{Q,i}) \cdot x + Const$,

g) As derived in Eq.(2.10) one expects a linear relation between the quadrupole gradient and current. Determine the current calibration constant C_g by a linear regression $\frac{\partial B_y}{\partial x} = C_g \cdot I_Q + Const$, as illustrated in Fig.1b

h) Repeat all steps a)-g) for the other transverse direction. For this one needs to rotate the Hall probe manually by 90 °. The movement in c) should be in the vertical direction and $B_x(y)$ has to be measured.

Task: 3 Effective length of a quadrupole

The goal of the experiment is to determine the effective length of the quadrupole, L_{eff}, which in turn affects the focal length, as shown in Eq. (2.13). For this measurement the quadrupole current is set to a high value, e.g. I_Q =2.5 A. The Hall probe is positioned off-center, e.g. at x =10 mm and y =0 mm so that only the vertical component of the magnetic field B_y has to be considered. One measures the dependence $B_y(z)$ i.e. B_y along the longitudinal position of the Hall probe as illustrated in Fig.1c. Ideally, one would measure over a wide longitudinal range, with the magnetic field dropping to zero at both ends, as illustrated in the inset of Fig.1c. However, due to the mechanical limitations of the positioning arm, only half of that range can be covered in practice. Fortunately, thanks to the symmetry of the longitudinal distribution, this is not a problem and the effective length can be determined as follows

$$L_{eff} = \frac{1}{B_0}\int_{-\infty}^{\infty} B(z)dz = \frac{2}{B_0}\int_{-\infty}^{z_0} B(z)dz \tag{1}$$

where z_0 is the longitudinal position of the maximum of the magnetic field and B_0 its maximum value.

Task: 4 Beam-based alignment

Ideally, the electron beam in an accelerator would cross a quadrupole at its magnetic center. As given by Eq.(2.4), at the point $x = 0, y = 0$ the field vanishes and the beam experiences no net force. If the beam has a slight offset $(\delta x, \delta y)$ relative to the center of the magnetic field, i.e. when $x = \delta x \neq 0, y = \delta y \neq 0$, then in addition to the focussing effect, the beam gets bent in the magnetic field $\vec{B} = (-g \cdot \delta y,\ -g \cdot \delta x,\ 0)$ in accordance to Eq.(2.4). The goal of this experiment is to determine the offsets $(\delta x, \delta y)$. In contrast to the previous Tasks, this one will be done with electron beam (therefore *beam-based*) and not in the magnetic measurement laboratory. Consider the setup sketched in Fig.1d. The electron beam passes through a quadrupole with an effective length of L_{eff} and a horizontal offset of δx relative to the magnetic center. The quadrupole is identical to the one previously characterized in the laboratory. An observation screen located at a distance L_D downstream the quadrupole can measure the horizontal position x of the beam. For simplicity's sake, assume only a horizontal offset δx (i.e. $\delta y = 0$) and $L_{eff} \ll L_D$. If the momentum p of the beam is known then the bending angle α can be calculated with the help of Eq.(2.2) as follows:

$$\alpha \approx \frac{L_{eff}}{R} = \frac{e \cdot L_{eff} \cdot B}{p} = \frac{e \cdot L_{eff} \cdot C_g \cdot I_Q \cdot \delta x}{p} \tag{2}$$

Here one makes use of the current calibration C_g, which has been determined in the previous Task. The geometry sketched in Fig.1d yields

$$x = x_0 + L_d \cdot \tan(\alpha) \approx x_0 + L_d \cdot \alpha = x_0 + L_d \cdot \frac{e \cdot L_{eff} \cdot C_g \cdot I_Q \cdot \delta x}{p} \tag{3}$$

and hence

$$\frac{dx}{dI_Q} = L_d \cdot \frac{e \cdot L_{eff} \cdot C_g \cdot \delta x}{p} \tag{4}$$

$$\boxed{\delta x = \frac{p \cdot \frac{dx}{dI_Q}}{e \cdot L_{eff} \cdot L_D \cdot C_g}} \tag{5}$$

Equation (5) above, suggests the following experimental procedure:

a) Set a current $I_{Q,i}$ through the quadrupole,

b) Measure the beam position x_i on the observation screen,

c) Repeat a)-b) for a different quadrupole current until there are at least 5 measure points,

From the slope of the linear fit $x_i(I_{Q,i})$ and Eq.(5) determine the quadrupole offset δx. Since the screen measurement allows for simultaneous measurement of the X and Y positions, the vertical offset can be determined in the same way.

Task: 5 Beam energy measurement using a dipole magnet

The measurements of electron beam momentum are based on Eq.(2.2) and use a dipole magnet, which bend the beam on a certain angle α. At AREAL a 90 ° bending magnet is used for this purpose. The dipole magnet bends the electron beam, and the beam position is registered by the YAG station (see energy spectrometer in Fig. 5.1). Thus the beam momentum can be determined by

$$p\left[\frac{\text{MeV}}{c}\right] = 0.02888 \cdot B[mT] \tag{6}$$

The momentum measurement together with the dipole field calibration is fully integrated in the accelerator control system of AREAL, therefore this task requires only electron beam transport to the observation screen and documentation of the operating conditions. Once the beam momentum has been measured, determine the mean beam energy.